Sensors & Diagnostics

ROYAL SOCIETY OF CHEMISTRY

CRITICAL REVIEW

View Article Online
View Journal | View Issue

Cite this: *Sens. Diagn.*, 2022, **1**, 627

Metal complexes for the visualisation of amyloid peptides

Jean-François Morfin,[a] Sara Lacerda,[a] Carlos F. G. C. Geraldes[bc] and Éva Tóth *[a]

Received 16th February 2022,
Accepted 1st April 2022

DOI: 10.1039/d2sd00026a

rsc.li/sensors

Amyloid forms of many different proteins have been long identified as relevant biomarkers in important pathologies with high societal impact, including Aβ in Alzheimer's disease, amylin in type 2 diabetes, α-synuclein in Parkinson's disease, *etc.* With over eighty novel complexes reported in the last six years, metal-based agents designed for the detection of such amyloid fibrils represent a rapidly growing field in molecular imaging. While the majority of these examples are radiocomplexes for nuclear imaging and focus on the detection of Aβ in Alzheimer's disease, there is increasing interest in other peptides and pathologies, and few studies are also directed at magnetic resonance imaging probes. In this review, we survey the recent literature according to the chemical nature of the amyloid recognition moieties, most of which are derived from a few basic structures, including benzothiazole, benzofuran or stilbene. Relationships between chemical structure and amyloid binding properties and biodistribution, in particular brain delivery and brain clearance, are outlined in order to help further work in this emerging area of research.

Introduction

In living systems, proteins can adopt various interconverting conformational states. Among these, amyloids refer to protein aggregates characterized by the presence of β-sheets and a fibrillar morphology. Amyloid formation of proteins has been first associated with a number of pathologies, like Alzheimer's and Parkinson's diseases or type 2 diabetes,

[a] *Centre de Biophysique Moléculaire, CNRS, UPR 4301, Université d'Orléans, Rue Charles Sadron, 45071 Orléans Cedex 2, France. E-mail: Eva.JAKABTOTH@cnrs.fr*
[b] *Department of Life Sciences and Coimbra Chemistry Centre, Faculty of Science and Technology, University of Coimbra, Calçada Martim de Freitas, 3000-456 Coimbra, Portugal*
[c] *CIBIT/ICNAS, University of Coimbra, Azinhaga de Santa Comba, 3000-548 Coimbra, Portugal*

Jean-François Morfin

Jean-François Morfin obtained his PhD in 2008 from the Université de Bretagne Occidentale, Brest, France, on the synthesis of macrocyclic polyamine derivatives as bismuth(III) chelators for alpha-immunotherapy applications. Then he moved as a postdoc to the Centre of Molecular Biophysics (CBM) in Orléans (2009–2011), where he studied the kinetics of gallium(III) complexation with NOTA and developed multimodal probes for amyloid visualization. He finally joined CBM as a CNRS research engineer in 2011 and is currently working on the development of molecular imaging probes based on metal complexes for biomedical applications.

Sara Lacerda

Sara Lacerda received her PhD from the University of Lisboa (2009), during which she developed and studied in vitro and in vivo theranostic agents. Later, she did a short postdoc at the University of Lübeck, Germany, on Fragment-Based Drug Discovery. In 2010–2012, her research focused on bimodal optical/MRI lanthanide-based lipo-nanoparticle contrast agents, at Centre de Biophysique Moléculaire (CBM), Orléans, France. From 2013 to 2015, she worked as a Research Associate at KCL's Imaging Sciences Division, London, UK, on new PET/MRI targeted probes for cardiovascular diseases. In 2016 she rejoined CBM as a CNRS Researcher. Her current project focuses on multimodal peptide-based contrast agents.

involving amyloid Aβ, α-synuclein (α-syn) and islet amyloid polypeptide (IAPP or amylin), respectively. While in these pathological cases, amyloid formation is detrimental to protein function, amyloid structures are also observed under normal physiological conditions and fulfil functional roles in biology.[1] Today it is thus accepted that the ability to form amyloid fibrils can be considered as an inherent property of polypeptide chains.

Amyloidogenesis, as depicted in Fig. 1, refers to the process of amyloid formation, when correctly folded proteins unfold or misfold, and in the absence of appropriate recognition of this state by protein quality control and degradation mechanisms, they misassemble into soluble and insoluble toxic oligomer/polymer cross-β-sheet fibrillary aggregates. Natively unfolded or intrinsically disordered proteins can also undergo aggregation. Amyloidogenesis is a multi-step process.[1,2] Early aggregates involve a limited number of molecules which still partially retain their original conformation and are kept together by weak intermolecular interactions. The internal reorganization of these small clusters can then lead to larger and more compact aggregates, characterized by extended β-sheets conferring higher stability to them. Their further growth *via* self-association or monomer addition gives rise to large, ordered, fibrillary structures. In other cases, amorphous or native-like aggregates can form respectively from disordered or native-like assemblies. Monomers, oligomers and fibrils typically coexist in equilibrium. These are further complexified by the possible fragmentation of the already formed fibrils into smaller units which can in turn initiate secondary nucleation.

In amyloid-related pathologies, amyloidogenesis is an important molecular signature of the disease which is directly associated with cell/organ dysfunction. It triggers lethal effects, such as ubiquitin proteasome system failure, lipid membrane permeability, oxidative stress, endoplasmic reticulum stress and mitochondrial dysfunction, leading to cell death. While fibrils are the end product of this process, they do not necessarily represent the most toxic form.

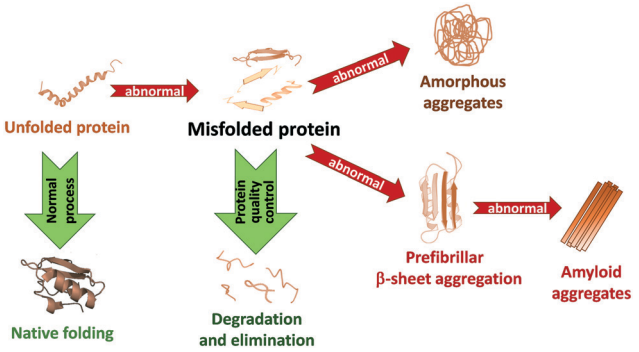

Fig. 1 Main processes of amyloidogenesis.

Molecular imaging aims at visualizing molecules, molecular processes and physical–chemical parameters in tissues or cells, in order to assess physiological or pathological phenomena or to diagnose diseases and monitor their evolution. In the context of amyloid-related diseases, much attention has been devoted to the detection of amyloid protein structures. Indeed, as amyloidogenesis occurs before the earliest clinical signs of the diseases, amyloids are generally considered as highly relevant biomarkers. In the past two decades, important efforts have been made to develop molecular imaging agents that specifically recognize amyloid peptides.

The scope of this review is to present the most recent developments in the field of molecular imaging of amyloid-related pathologies. After a short description of relevant amyloid-forming peptides, we will specifically focus on the design of metal-based agents which are highly versatile as

Carlos F. G. C. Geraldes

Carlos Geraldes has been Full Professor at the University of Coimbra, Portugal, since 1988, retired and invited Professor since 2018. He received a PhD degree in Inorganic Chemistry at the University of Oxford, UK. He was a Fulbright scholar in the US, is a Fellow of the Lisbon Academy of Sciences and received several scientific prizes. His current research interests include inorganic contrast materials for MRI and molecular imaging. He co-authored 310 articles and 15 book chapters (h factor of 50), which have received over 9000 citations.

Éva Tóth

Éva Tóth is an expert in the chemistry of metal complexes for imaging applications. After a PhD from the University of Debrecen, Hungary, she occupied research positions at EPF Lausanne, Switzerland. In 2005, she became CNRS research director in the Centre of Molecular Biophysics, Orléans, France. She published over 180 papers, 16 book chapters and edited The Chemistry of Contrast Agents in Medical Magnetic Resonance Imaging (Wiley). In 2019, she became an external member of the Hungarian Academy of Sciences. Her recent work focuses on the design of responsive MRI probes and Mn alternatives to clinical Gd-based contrast agents.

they can provide detection capability in different imaging modalities as a function of the metal ion selected. The same chelating ligand can be complexed to different radioisotopes or other metal ions and provide probes detectable in various modalities (*e.g.* $^{64}Cu^{2+}$ and $^{68}Ga^{3+}$ for positron emission tomography (PET), $^{111}In^{3+}$ for single-photon emission tomography (SPECT), Gd^{3+} for magnetic resonance imaging (MRI), *etc.*). On the other hand, most of the examples are derived from a few basic amyloid-targeting moieties such as benzothiazole, benzofuran or stilbene, and there are relatively scarce data with other types of recognition units. The majority of the agents target amyloid Aβ in the context of Alzheimer's disease or more recently amylin in diabetes, while very few examples treat other amyloid peptides. Since the chemical design and the nature of the recognition moieties are essentially independent of the peptide targeted, we propose here to survey the literature, from the past six years, by classifying the most representative examples according to the chemical structure of their targeting function. While our review does not intend to be fully exhaustive, we want to illustrate advances specifically in the following areas: (i) improving the affinity to amyloid peptides *via* structural optimization and understanding how affinity is affected by the solution behaviour of the amphiphilic chelates; (ii) relating organ (brain and pancreas) uptake and clearance to the molecular structure; and (iii) *in vivo* preclinical validation to achieve best contrast between diseased and healthy tissue.

Amyloids, related human diseases and their detection by molecular imaging

Basic properties of amyloid peptides and proteins and related diseases

Amyloidogenesis of normally soluble proteins has so far been found to be a hallmark of about 30 highly debilitating human diseases. Modern structural biology techniques have contributed to a dramatic increase in detailed structural information on amyloid fibrils. This knowledge helps understand the molecular basis of the diseases and enables the rational design of new, more specific molecular imaging probes. Although amyloid beta (Aβ) peptide and amylin have been the only targets in molecular imaging, hopefully, others will also attract attention in the future.

The amyloid precursor protein (APP) is a 100–140 kDa transmembrane glycoprotein that plays a major role in the pathogenesis of Alzheimer's disease (AD), the most common neurodegenerative disease. In healthy individuals, APP cleavage by α-secretase generates a C83 carboxy-terminal fragment and soluble APP, which is associated with normal synaptic transmission. In the diseased state, APP is abnormally cleaved first by β-secretase and then γ-secretase, releasing from the cell membrane amyloid beta (Aβ) peptides containing predominantly 39–42 amino acid residues. The longer Aβ species, particularly $Aβ_{1–40}$ and $Aβ_{1–42}$, aggregate into neurotoxic soluble oligomers in the extracellular space. Accumulation of $Aβ_{40/42}$ inhibits ion channels, impedes calcium homeostasis, and impairs neuronal energy metabolism, eventually leading to neuronal cell death. These oligomers aggregate in turn into larger insoluble β-sheet fibrils (8–10 nm) and ultimately into dense fibrillary amyloid plaques, the main hallmark of AD.[3] The deposition of amyloid beta peptide on the walls of small to medium blood vessels of the central nervous system and meninges leads to a form of angiopathy called cerebral amyloid angiopathy (CAA), which is a major factor in intracerebral haemorrhage and vascular cognitive impairment.[4]

Amylin, or islet amyloid polypeptide (IAPP), is a peptide hormone co-secreted with insulin from pancreatic β-cells in response to food intake. It has an important role in the regulation of glycemia, preventing spikes in blood glucose levels after meals by slowing gastric emptying and promoting satiety. Amylin is produced by post-translational modifications, including protease cleavage, from the 67 amino acid pro-IAPP produced in the pancreatic β-cells. Human IAPP has 37 amino acid residues, with a disulfide bridge between cysteines 2 and 7. IAPP can adopt an α-helical structure at residues 8–18 and 22–27 and can form dimers, which is an early step in fibril formation. IAPP can also form heterodimers with insulin. While dimerization of IAPP accelerates fibril formation, insulin blocks it by blocking the IAPP dimerization interface. The early prefibrillar structures are more toxic to β-cells than the later ones. Amyloid deposition of amylin in pancreatic islets (islet amyloid) is characteristic of type 2 diabetes (T2D), the most common form of diabetes mellitus (about 90%), which is closely associated with number reduction and dysfunction of β-cells.[5]

The tau (τ) protein is a microtubule-associated, intrinsically disordered protein (IDP) which is mainly expressed in the axons of central nervous system neurons. Tau protein monomers, with 352–441 amino acid residues, have an N-terminal projection domain and a C-terminal microtubule-binding domain, which share a central proline-rich region. In healthy neurons, tau promotes the assembly and the stabilization of microtubules through tubulin-binding motifs in the microtubule-binding domain. Hyperphosphorylated tau protein dissociates from the neuronal microtubules, misfolds and aggregates, forming highly structured amyloid fibrils, which lead to the formation of intracellular insoluble aggregates called neurofibrillary tangles (NFTs). These intracellular NFT aggregates of tau define a group of neurological disorders known as tauopathies, such as AD, but are also present in amyotrophic lateral sclerosis (ALS) and Pick's disease, among others.[6]

α-Synuclein is a small (140 amino acid residues) soluble protein that normally exists in a natively unfolded state, localized in the nucleus of brain neurons. In Parkinson's disease (PD), the second most common neurodegenerative disorder, abnormal α-syn accumulation occurs in intra- and inter-neuronal inclusions (Lewy bodies and Lewy neurites, respectively), which leads to degeneration of substantia *nigra*

dopaminergic neurons. In PD, the conformation of α-syn changes to α-helical fibrils and oligomers that form β-sheet rich fibrils. Such protein aggregation is the basis for the "misfolded hypothesis" of PD. α-Syn has also been shown to be autoproteolytic, generating a variety of low molecular weight fragments. Those containing the NAC region (non-amyloid β component, residues 61–95) undergo faster aggregation than α-syn and may play a role as intermediates or cofactors in the *in vivo* aggregation of α-syn. α-Syn aggregates can also migrate from affected to unaffected neurons, causing further misfolding.[7]

Human Cu–Zn superoxide dismutase (SOD1) is a 16 kDa protein, normally forming a 32 kDa homodimer. The structure of each SOD1 subunit consists of a β-barrel core and seven loops which are held together by an intramolecular disulfide bond, a binuclear Cu^{2+}/Zn^{2+} metal binding site and a global hydrogen bond network. SOD1 is mainly distributed in the cytoplasm but is also found in the nucleus, lysosomes and mitochondria. Its main function is to dismutate superoxide radicals ($O^{2\cdot-}$) into molecular oxygen (O_2) and the less reactive hydrogen peroxide (H_2O_2), thus eliminating the free radicals that cause oxidative stress. Mutant SOD1 proteins, some of which originate from oxidative stress, aggregate more extensively than the normal wild-type (wt) SOD1 protein. Amyotrophic lateral sclerosis (ALS) is a fatal adult-onset neurodegenerative disorder characterized by progressive degeneration of upper motor neurons in the motor cortex and lower motor neurons in the spinal cord and brainstem. Hallmarks of ALS include mutant SOD1 protein aggregates, mainly found in spinal motor neurons. Increased aggregation, dimer destabilization and oligomerization are mechanisms proposed for mutant SOD1 toxicity.[8]

The TAR DNA-binding protein 43 (transactive response DNA-binding protein 43 kDa, TDP-43) in its full-length form is a dimer formed by interaction between two N-terminal domains, and this dimerisation can be propagated to form higher-order oligomers. Protein mutations located in the glycine-rich region of TDP-43 and their accumulation contribute to the development of ALS. A hyper-phosphorylated, ubiquitinated and cleaved form of TDP-43, known as pathologic TDP-43, mislocalized in the cytoplasm, is also a key pathological feature of other major neurodegenerative diseases, including AD, PD and Huntington's disease (HD).[9]

Beta-2 microglobulin (B2M) is a 17 kDa ubiquitously expressed protein present on all nucleated cells. It is organised in a β-sandwich fold with seven antiparallel β-strands. pH-dependent aggregation (more extensive at acidic pH) of this protein is often a problem during kidney dialysis. In patients undergoing long-term haemodialysis, B2M can aggregate into amyloid fibers that damage the kidneys' glomeruli, which become unable to filter out B2M, leading to high blood levels and dialysis-related amyloidosis (DRA).[10]

In its wild-type form, the huntingtin (HTT) protein (348 kDa) contains 6–35 glutamine residues. The isolated protein is believed to be intrinsically disordered. Studies of the HTT-associated protein 40 (HAP40) complex showed that HTT is largely α-helical and consists of three major domains.[11] The amino- and carboxy-terminal domains contain multiple HEAT (huntingtin, elongation factor 3, protein phosphatase 2A and lipid kinase TOR) repeats arranged in a solenoid fashion. HTT is essential for embryonic development and is involved in diverse cellular activities such as vesicular transport, endocytosis, autophagy and the regulation of transcription, ensuring normal development before birth. It is expressed in many tissues, with the highest extent in the brain.[12] In Huntington's disease (HD), mutated HTT contains more, up to 250, glutamine residues, leading to abnormal neuronal aggregation. Recently, HD has also been associated to tau aggregation.[13]

The prion protein (PrP) is mostly expressed in the nervous system. Human PrP (PrP^C) is possibly involved in Cu^{2+} transport to cells, in cell signalling or in the formation of synapses. The protein can exist in multiple isoforms, the normal PrP^C and misfolded protease-resistant forms, such as the disease-causing PrP^{Sc} (scrapie). Normal PrP^C has 43% α-helical and 3% β-sheet content, whereas PrP^{Sc} possibly has a total β-sheet composition. Brain accumulation of the misfolded PrP^{Sc} is associated with cognitive disorders and neurodegenerative diseases such as ovine scrapie, bovine spongiform encephalopathy (BSE, mad cow disease) and human Creutzfeldt–Jakob disease (CJD). The predominant hypothesis for the propagation of PrP^{Sc} is that the change from normal PrP^C is caused by the presence of and interaction with PrP^{Sc}.[14]

Transthyretin (TTR) is a transport protein found in the serum and cerebrospinal fluid that transports the thyroid hormone thyroxine (T4) and retinol-binding protein bound to retinol. TTR is a homo-tetramer where each monomer is a 127-residue polypeptide rich in β-sheet structures. Two monomers associate *via* their edge β-strands to form an extended β-sandwich and two of these dimers associate face-to-face to produce the homo-tetrameric structure and create two thyroxine binding sites per tetramer. TTR misfolding and aggregation into amyloid fibrils is associated with the slowly progressing, adult-onset diseases senile systemic amyloidosis (SSA), familial amyloid polyneuropathy (FAP) and familial amyloid cardiomyopathy (FAC). TTR point mutations destabilize the tetramer with mutant and wt-TTR subunits and facilitate misfolding and amyloidogenesis, leading to TTR amyloid deposition in the extracellular space. The severity of the disease varies greatly with the mutation site.[15]

Molecular imaging modalities for *in vivo* amyloid detection

Molecular imaging can play a central role in the early *in vivo* detection of misfolded protein aggregates considered as specific disease biomarkers. This is important for accurate diagnosis, for improved understanding of molecular and cellular mechanisms underlying the diseases and for the monitoring of novel therapeutic approaches. The currently

available preclinical and clinical imaging modalities for amyloid detection include magnetic resonance imaging (MRI), positron emission tomography (PET), X-ray computed tomography (CT), single-photon emission CT (SPECT), optical imaging (OI), ultrasound (US) imaging and photoacoustic imaging (PAI). Among these, MRI displays high resolution and has the advantage of being non-invasive and non-ionising, but has poor sensitivity. PET, SPECT and OI, on the other hand, provide high sensitivity. Two or more modalities can be combined in multimodal imaging to potentiate their advantages and overcome their limitations, providing more accurate diagnostics. Modalities with high spatial resolution (MRI/CT) are ideally combined with highly sensitive modalities (OI/nuclear imaging) to complement anatomical with molecular/functional information.[16,17] Detailed descriptions of the imaging techniques can be found elsewhere.[16,18] Amyloid-targeted probes have been developed for most of these imaging modalities and surveyed in previous reviews by us[19] and others.[20,21] Among all, PET has been the most widely used technique for both clinical and pre-clinical imaging of amyloid plaques, especially in the framework of AD, mainly thanks to the successful use of ^{18}F- or ^{11}C-labelled probes based on Pittsburgh compound B (PiB) or other small molecules (Scheme 1).[20] In addition to their good amyloid binding properties, their small size and lipophilic character are important for sufficient passage *via* the blood–brain barrier (BBB), which constitutes an important obstacle in brain imaging.

Targeted probes for amyloid detection

Probes based on benzothiazole derivatives (Table 1)

Building on the early success of PiB in targeting Aβ plaques, a vast majority of metal-based imaging probes are based on benzothiazole derivatives. Benzothiazole moieties are inspired from thioflavin S and T, well known to bind amyloid deposits. Their structure can be easily modulated.

A first class of benzothiazole-based probes involves cyclopentadienyl Re/^{99m}Tc tricarbonyl complexes. Their low molecular weight, small size and high stability are interesting features for BBB crossing and thus brain imaging, but these complexes present only moderate affinities to Aβ plaques.

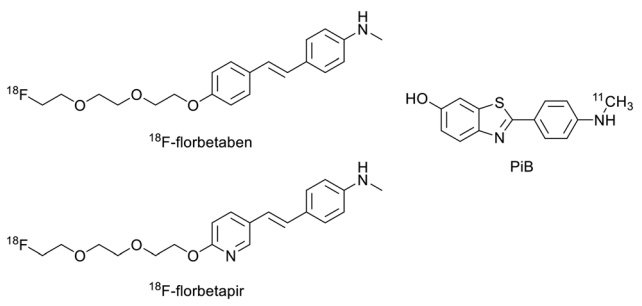

Scheme 1 ^{18}F- or ^{11}C-labelled PET probes.

In 2016, J. Jia *et al.* synthetized a series of ^{99m}Tc/Re-labeled cyclopentadienyl tricarbonyl derivatives linked to 2-phenyl/pyridylbenzothiazole *via* an ester function and an alkyl chain (ML1–8, Scheme 2).[22] In these structures, the ester function was described to facilitate BBB crossing, as compared to an amide, by limiting hydrogen bonds. The lipophilicity could be modulated through the alkyl chain length and the pyridyl/phenyl substitution. Surprisingly, these structural modifications did not prove to have a major impact on the lipophilicity, since all the ^{99m}Tc complexes had $\log P_{oct/PBS}$ between 2.69 and 2.99, but showed different affinities to $A\beta_{1-42}$ aggregates. The affinity of the phenylbenzothiazole derivatives ML1–4 was higher (in the 12–25 nM range) than those of the pyridylbenzothiazole analogues ML5–7 (in the 42–204 nM range), except in the case of the pentyloxy linker with the *N*,*N*-dimethylated form ML8 (15 nM) (Table 1). The general tendency indicated that higher affinity was achieved with the longest linker and the phenyl group. Unfortunately, *in vivo* biodistribution in normal mice demonstrated that despite their small size, these probes were not able to cross effectively the BBB.

Kiritsis *et al.* also designed a ^{99m}Tc cyclopentadienyl complex (^{99m}TcL9) for SPECT imaging of Aβ plaques (Scheme 2).[23] The complexing unit was directly linked to a 2-(4′-aminophenyl)-benzothiazole through an amide function, reducing the molecular size compared to those of Jia *et al.* These complexes (^{99m}Tc and its Re analogue) demonstrated suitable lipophilicity for BBB crossing ($\log P_{oct/water}$ = 2.35) and also bound $A\beta_{1-42}$ aggregates with high affinity (K_i = 13.6 nM). Despite these properties, the brain uptake measured in biodistribution studies in normal mice was moderate (0.53% ID per g at 2 min) with a clearance ratio 2/90 min of 2.1. In 7 month old transgenic mice (5xFAD), even if the brain uptake at 2 min was the same, a significant increase (1.94% ID per g) was observed at 90 min due to the presence of β-amyloid plaques, thus probe retention.

In 2019, the same group developed ^{99m}TcL10 wherein the cyclopentadienyl complexing unit was directly linked to the benzothiazole part (Scheme 2).[24] This radiocomplex presented a high stability in biological medium for 90 min and possessed improved properties for BBB crossing compared to ^{99m}TcL9: a smaller size and a higher lipophilicity ($\log P_{oct/water}$ = 2.52). It was confirmed in biodistribution studies in healthy mice by a very high brain uptake at 2 min (7.94% ID per g), respectively similar to and higher than that for the clinically used PET agents ^{18}F-florbetapir and ^{18}F-florbetaben.[20] Besides, the brain clearance ratio 2/90 min of 39.7 indicated no unspecific retention in brain tissues, which is an essential condition for an AD imaging probe. The authors also did biodistribution studies in transgenic 5xFAD mice and compared the results at 15 min to those obtained for wild-type animals. They noted an increase of the radioactivity detected (3.90% ID per g *vs.* 2.68% ID per g for the wild-type mice), attributed to the presence of Aβ plaques, which was confirmed by fluorescent staining with thioflavin S. The rhenium analogue bound

Table 1 Main properties of the benzothiazole derivative probes

Ligand number	Molecular weight of ligand	Metal	log *P* of complex	Targeted protein	Affinity to protein[a] (K_i, nM)	Brain uptake at 2 min[b] (% ID per g)	Ref.
1	405.5	Re/^{99m}Tc	2.69	$A\beta_{1-42}$	18.8	1.06/p: 4.04	22
2	433.6	Re/^{99m}Tc	2.84	$A\beta_{1-42}$	22.75	—	22
3	419.5	Re/^{99m}Tc	2.99	$A\beta_{1-42}$	12.39	0.70/p: 4.03	22
4	447.6	Re/^{99m}Tc	2.79	$A\beta_{1-42}$	22.26	—	22
5	406.5	Re/^{99m}Tc	2.81	$A\beta_{1-42}$	204.10	—	22
6	434.5	Re/^{99m}Tc	2.79	$A\beta_{1-42}$	42.04	0.69/p: 3.77	22
7	420.5	Re/^{99m}Tc	2.81	$A\beta_{1-42}$	130.63	—	22
8	448.6	Re/^{99m}Tc	2.69	$A\beta_{1-42}$	15.10	0.54/p: 4.11	22
9	317.4	Re/^{99m}Tc	2.35	$A\beta_{1-42}$	13.6	0.53/p: 1.70 AD: 0.52/p: 1.96	23
10	198.3	^{99m}Tc	2.52	$A\beta_{1-42}$	65.8	7.94/p: 6.99	24
11	494.6	Re	0.15	$A\beta_{1-40}$	—	—	25
12	518.8	Re/^{99m}Tc	2.88	$A\beta_{1-42}$	30.9	1.57	26
13	519.8	Re/^{99m}Tc	2.48	$A\beta_{1-42}$	102.6	0.92	26
14	509.6	^{64}Cu	0.97	$A\beta_{1-40}$	30*/275	0.17	28
15	523.7	^{64}Cu	0.72	$A\beta_{1-40}$	40*/325	1.33	28
16	567.9	^{64}Cu	0.64	$A\beta_{1-40}$	320*/2350	0.49	28
17	779.0	^{64}Cu	0.82	$A\beta_{1-40}$	580*/142	0.61	28
18	426.6	^{64}Cu	0.92	$A\beta_{1-40}$	170*/795	0.75	28
19	439.6	^{64}Cu	1.30	$A\beta_{1-42}$	—	0.99	29
20	439.6	^{64}Cu	1.08	$A\beta_{1-42}$	—	—	29
21	425.6	^{64}Cu	1.29	$A\beta_{1-42}$	—	0.16	29
22	440.6	^{64}Cu	0.58	$A\beta_{1-42}$	—	—	29
23	426.6	^{64}Cu	0.56	$A\beta_{1-42}$	—	—	29
24	679.9	^{64}Cu	1.09	$A\beta_{1-42}$	—	—	29
25	526.7	^{64}Cu	1.26	Aβ	—	0.35	30
26	512.7	^{64}Cu	1.07	Aβ	—	0.23	30
27	498.6	^{64}Cu	1.01	Aβ	—	0.32	30
28	484.6	^{64}Cu	0.91	Aβ	—	0.46	30
29	470.6	^{64}Cu	1.15	Aβ	—	0.23	30
30	642.7	Gd/^{111}In	−0.15	$A\beta_{1-40}$/amylin	$1.8 \times 10^{5\$}/1.54 \times 10^{5\$}$	0.86	31
31	755.9	Gd/^{111}In	0.03	$A\beta_{1-40}$/amylin	$6.7 \times 10^{4\$}/8.3 \times 10^{4\$}$	—	31
32	714.8	Gd	—	$A\beta_{1-40}$	$1.94 \times 10^{5\$}$/—	—	31
33	761.9	Gd	0.32	$A\beta_{1-40}$	—	—	31
34	755.9	Gd/^{111}In	0.63	$A\beta_{1-40}$/amylin	$5.1 \times 10^{3\$}/3.7 \times 10^{3\$}$	0.3/p: 2.9	34
35	812.0	Gd	1.46	$A\beta_{1-40}$/amylin	$4.4^{\$}/4.5^{\$}$	0.3/p: 3.7	34

[a] Metal complexes or * ligand; $^{\$}K_d$. [b] p = pancreas; AD = murine or rat model of Alzheimer's disease.

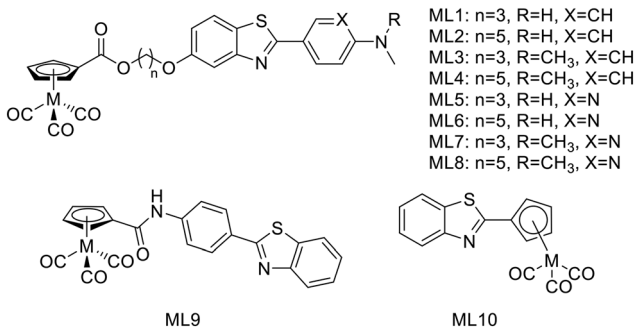

Scheme 2 ^{99m}Tc/Re-labeled cyclopentadienyl tricarbonyl derivatives linked to benzothiazole derivatives.

selectively plaques with a good affinity (K_i = 65.8 nM) and also exhibited theranostic properties such as inhibition of Aβ fibril formation and antioxidant activity.

Two other ^{99m}Tc complexes have been recently described with an N-heterocyclic carbene (NHC) (^{99m}TcL11) or bis(aminoethanethiol) (BAT) (^{99m}TcL12–13) scaffold by Wiratpruk *et al.*[25] and Zhang *et al.*,[26] respectively (Scheme 3). The first series of highly stable $Re(CO)_3$ complexes of bifunctional bis(NHC)-amine ligands coupled to benzothiazole had been synthetized before, with promising results of selective binding to amyloid plaques from human brain tissues, but potentially low BBB permeability because of their positive charge.[27] In the following work, the molecular design was improved by introducing a carboxylate function to form a neutral complex. However, the rhenium complex ReL11 became too amphiphilic ($\log P_{oct/water}$ = 0.15),

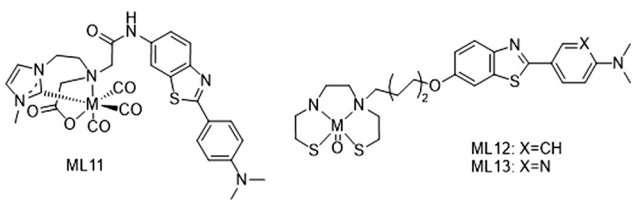

Scheme 3 ^{99m}Tc complexes with an N-heterocyclic carbene (^{99m}TcL11) or bis(aminoethanethiol) (^{99m}TcL12–13) scaffold.

which was not optimal for brain penetration and also reduced amyloid plaque binding in AD patient brain slices. This ligand system provides a good basis for further improvements, such as the replacement of the NHC methyl substituent by a more lipophilic *tert*-butyl or cyclohexyl group.

Zhang *et al.* linked the BAT chelator to a 2-phenyl/pyridylbenzothiazole through an oligoethyleneoxy spacer. The introduction of this pegylated moiety, instead of the alkyl chain in previously described analogues, was expected to reduce the lipophilicity of the Re/^{99m}Tc complexes and improve brain pharmacokinetics, namely the initial brain uptake and the clearance ratio from healthy brain. Both ReL12 and ReL13 presented specific and efficient binding to Aβ plaques from AD patients, and as observed by Jia *et al.*,[22] the presence of the phenyl in ReL12 instead of the pyridyl group in ReL13 led to greater affinity to $A\beta_{1-42}$ aggregates, with K_i = 30.9 nM and K_i = 102.6 nM, respectively. Biodistribution data in normal mice confirmed the benefit of the pegylated linker. Indeed, they showed increased initial brain uptake at 2 min as compared to the alkyl analogues as well as a good 2/60 min clearance ratio.

Among benzothiazole derivatives, a second class of β-amyloid imaging probes is composed of macrocyclic polyamine ligands. These chelators have the advantage of forming highly stable and kinetically inert complexes with various metals such as copper(II), gallium(III) or lanthanides(III), and can be easily functionalized to introduce an amyloid targeting unit.

For ^{64}Cu coordination, in 2017, Bandara *et al.* proposed a series of five new ligands L14–18, wherein a 2-(4-hydroxy)-3-methoxyphenyl-benzothiazole is linked to 2,4-dimethyl-1,4,7-triazacyclononane (TACN) or 2,11-diaza[3.3](2,6)-pyridinophane derivatives (Scheme 4).[28] The targeting unit was directly linked to the macrocycles through a Mannich reaction, and for the tetraamine derivatives, lipophilicity and charge were modulated *via* the R substituent (L14–16) or by adding a second benzothiazole unit (L17). The interactions between the ligands or the Cu complexes and the Aβ aggregates were studied *in vitro* and did not show dramatic variation upon metal complexation: all affinities remained in the nanomolar range, even if the Cu complexes of L14–16 and L18 exhibited 4–8 times lower affinities as compared to the corresponding ligand. The affinity decrease was the most visible for CuL16 that showed micromolar affinity (2.33 μM) due to the less positive charge of the metal complex *via* the deprotonation of the carboxylic acid function. For CuL17, an opposite behavior was observed. The 4 times higher affinity was attributed to a rearrangement of the two targeting units upon copper(II) coordination to allow for better interaction with the Aβ fibrils. *Ex vivo* experiments on brain slices of AD transgenic mice confirmed the specific binding of these probes to Aβ fibrils. Despite the $\log P_{oct/water}$ values inferior to 1, the complexes, in particular CuL14, were able to cross the BBB, exhibited promising initial brain uptake and rapid clearance in biodistribution studies in wild-type mice. MicroPET imaging studies on transgenic mice also confirmed the promising properties of these compounds as diagnostic tools for AD, even if their affinity and lipophilicity might be further improved.

In a follow-up work published in 2020, the same authors reported on another series of benzothiazole derivatives L19–24 as theranostic agents, wherein the targeting unit has been modified (Scheme 4).[29] They used PiB derivatives with a mono- or a dimethylamine group and introduced an additional hydroxyl group on the benzothiazole part. The replacement of the phenyl by a pyridyl group and the introduction of a hydrogen bond acceptor were also studied. These units were thus linked to methylated TACN macrocycle *via* the benzothiazole aromatic ring. These structural variations allowed for several conclusions. First, the affinity studies outlined the ability of all compounds to efficiently bind Aβ aggregates, but the monomethylated derivatives had higher specificity over the dimethylated analogues as well as reduced cytotoxicity. The pyridine derivative L22 and L23 ligands presented lower affinity but had improved antioxidant properties. Interestingly, L23 was able to strongly reduce neurotoxicity by accelerating the aggregation of toxic $A\beta_{1-42}$ oligomers into non-toxic $A\beta_{1-42}$ aggregates. All these ligands could be radiolabeled with ^{64}Cu for PET imaging, but

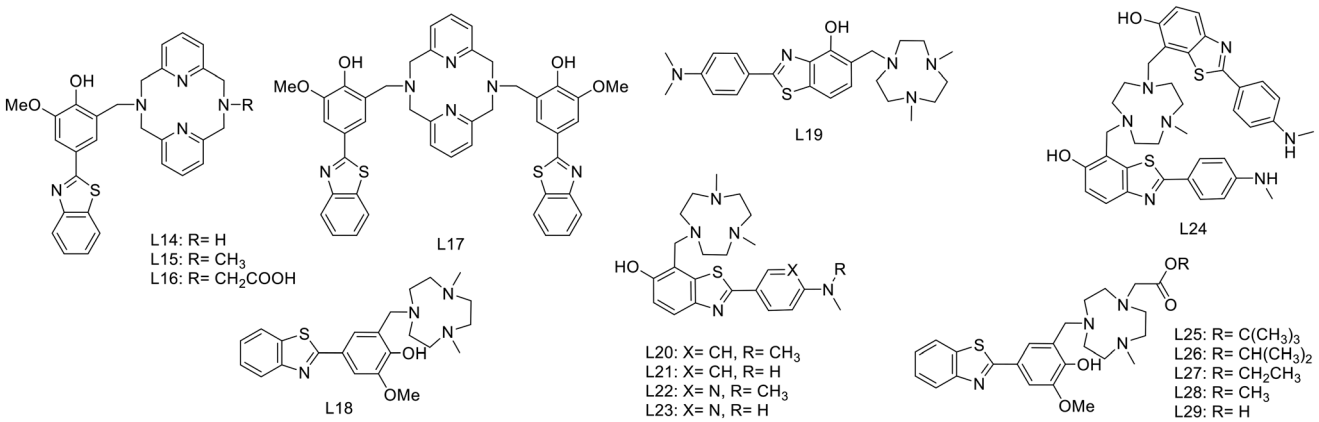

Scheme 4 Benzothiazole derivatives linked to macrocyclic ligands (2,11-diaza[3.3](2,6)-pyridinophane or TACN scaffolds) for ^{64}Cu coordination.

among all complexes, only CuL19–21 and CuL24 showed suitable lipophilicity and amyloid binding in transgenic mice brain sections. CuL20 had poorer amyloid binding specificity. In the case of CuL24, the second benzothiazole unit did not improve the binding properties, and the reduction of lipophilicity and the increase of the molecular weight were not favorable for BBB crossing. CuL19 and CuL21 were finally included in an *in vivo* biodistribution study in normal mice and showed very different behavior. The initial brain uptake was good for CuL19 (0.99% ID per g at 2 min) but much lower for CuL21 (0.16% ID per g at 2 min). The authors related this to the different position of the hydroxyl group on the benzothiazole ring (position 4 *vs.* 5). Overall, these probes were considered as very promising for combined therapy and PET imaging in Alzheimer's disease. Fig. 2 illustrates the autoradiography of the uptake of ML19–21 and ML24 in WT and AD transgenic mice and in transgenic mice in the presence of a known Aβ blocking agent.

Lately, the same group published a novel series of potential ^{64}Cu PET imaging probes derived from L18 by substituting one methyl group on the TACN macrocycle with an acetic acid (L29) or with various alkyl carboxylate esters (L25–28) (Scheme 4).[30] These structural modifications allowed for increased stability of the Cu^{2+} complex without affecting the amyloid binding properties. Indeed, CuL25 and CuL28 presented remarkable affinities and high specificity for amyloid plaques. The lipophilicity of these ^{64}Cu complexes was in the same range as those of the previous compounds ($\log P_{oct/PBS}$ between 0.9 and 1.3), while the biodistribution studies showed moderate initial brain uptake (0.23–0.46% ID per g) and rapid clearance for all complexes, indicating that free copper(II) was not released in the brain.

For a decade, our group has been developing metal complexes as potential imaging agents for amyloid Aβ or amylin detection. These probes consist of 3 parts: (i) a macrocyclic chelator based on DOTA providing high affinity for lanthanides and strong kinetic inertness, (ii) a PiB derivative as the targeting unit and (iii) a neutral spacer. Such ligands can be suitable for different imaging techniques by complexing the appropriate metallic ion (Gd^{3+} for MRI, In^{3+} for SPECT and Ga^{3+} for PET).[31–34]

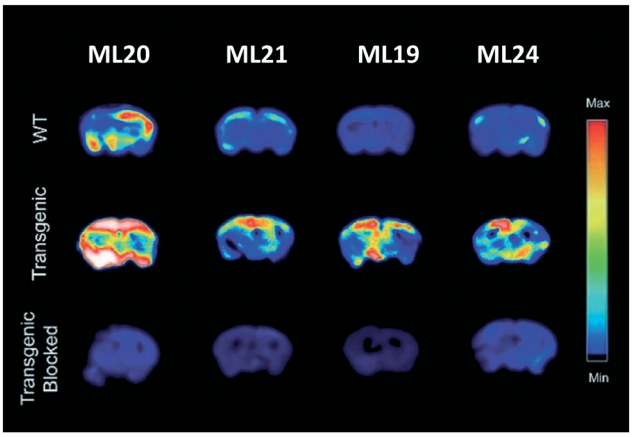

Fig. 2 Autoradiography of brains from WT and AD transgenic mice upon injection of ML19–21 and ML24, in the absence and presence of a known Aβ blocking agent. Reproduced from ref. 29 with permission from RSC. Copyright 2020.

We modulated the length and the nature of the linker, the orientation of the PiB unit and the global charge of the Ln^{3+} complexes by using DO3A monoamide or DOTAGA derivatives (Scheme 5). The first generation of these complexes (L30–33) presented an affinity to $A\beta_{1-40}$ aggregates of K_d = 67–194 μM, determined by SPR. The slightly weaker affinity of LnL32 indicated that a negative global charge is less favorable for binding. The presence of the metal complex drastically deteriorated the binding properties of the PiB unit, since the dissociation constants were five orders of magnitude lower than for the PiB itself.

The influence of these first-generation probes on $A\beta_{1-40}$ aggregation was studied by several techniques (UV-vis spectroscopy, circular dichroism (CD), dynamic light scattering (DLS) and transmission electron microscopy (TEM)). We could conclude that even small structural variations between LnL30, LnL31 and LnL32 were important, as they could either promote (LnL30 and LnL32) or inhibit $A\beta_{1-40}$ fibril formation (LnL31). Regardless of the low lipophilicities, the initial brain uptake (0.36 and 0.5% ID per g in the cortex and in the cerebellum at 2 min) and the rapid clearance observed for ^{111}InL30 in adult male WT mice were quite promising for potential nuclear imaging.

Despite these interesting initial results, the lipophilicity of the probes for better BBB permeability as well as their amyloid binding affinity needed improvement. We therefore developed a second generation of ligands wherein we changed the orientation of the PiB unit and used longer alkyl spacers (with six or ten carbons). To further increase the lipophilic character, we removed an amide function and dimethylated the amine in the PiB moiety (Scheme 5).

The first study using ^{111}InL31 and ^{111}InL34 complexes confirmed the gain in lipophilicity.[33] The neutral complex GdL34 exhibits a more favorable $\log P_{oct/water}$ of 0.63 but showed similarly low brain uptake to ^{111}InL31 and ^{111}InL34 (0.07 *vs.* 0.12% ID per g at 30 min post injection) in healthy mice. The increased molecular weight resulting from the longer alkyl chains was likely a limiting parameter for the BBB crossing.

Brain delivery of our Gd-complexes could be improved *via* conjugation to nanocarriers capable of translocating across the BBB – either *per se* or upon targeting to transporters expressed in the brain vasculature. Previous *in vitro* and *in vivo* proof-of-concept studies demonstrated that functionalized multi-walled carbon nanotubes (f-MWNTs) were capable of crossing an intact BBB. A significant improvement of brain accumulation was observed for ^{111}InL31 conjugated to f-MWNTs-NH^{3+}, with a whole-brain uptake of ~1.16% ID per g of tissue, corresponding to a ~10-fold increase compared to the free chelate.

Due to their large size and the hydrophilic character of the chelate part, metal complexes conjugated to amyloid

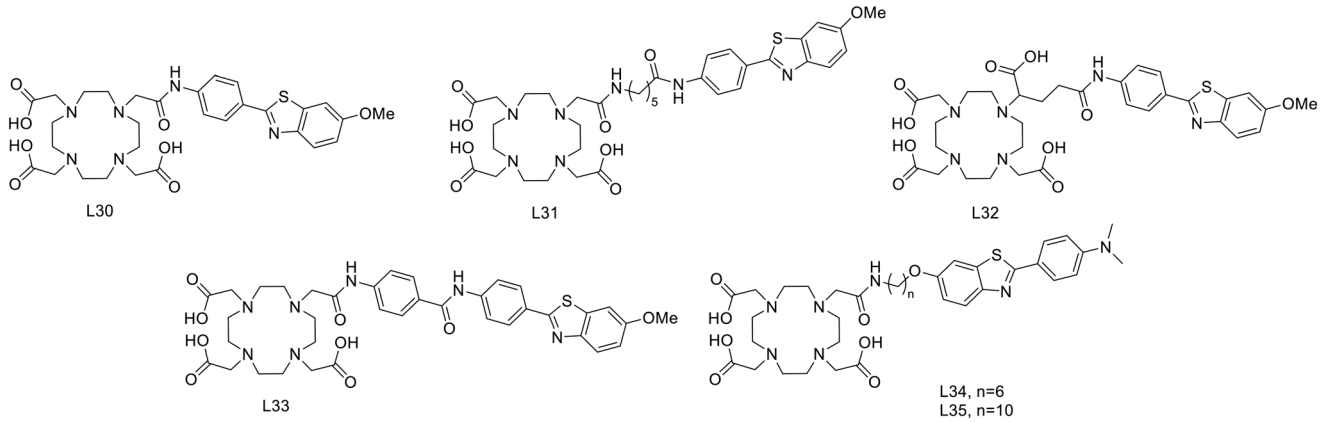

Scheme 5 PiB-conjugated DO3A monoamide or DOTAGA derivatives for Ln^{3+} and $^{111}In^{3+}$ complexation.

targeting units exhibit poor brain penetration, which prevents their efficient use for MRI imaging of Alzheimer's disease. This is especially true given the low sensitivity of MRI detection which requires orders of magnitude higher probe concentrations than nuclear imaging.

Therefore, it seems important to envisage more accessible biomarkers. Amylin deposits are localized in pancreatic islets, where Gd^{3+} complexes could reach the target more easily and in larger quantities. In this regard, we have recently investigated the binding properties of GdL30–31 and GdL34–35 towards amylin in comparison with $A\beta_{1-40}$ aggregates.[34] Their binding affinities were characterized by SPR with aggregated $A\beta_{1-40}$ and amylin. With a standard level of peptide immobilization on the SPR chips (~4000 RU), favorable to minimize steric effects and non-specific interactions, the dissociation constants of each complex were in the μM range. No peptide selectivity was observed for any of the complexes; the K_d values were similar for $A\beta_{1-40}$ and amylin fibrils. The results showed a clear tendency with respect to structural modifications of the ligand: as expected, the affinity becomes higher when the PiB unit is farther away from the metal complex. This was further confirmed by SPR using very high peptide immobilization levels (~9000 RU) which can allow for better SPR sensitivity and the assessment of interactions at very low GdL concentrations. Under these conditions, an additional interaction in the nM concentration range was identified for GdL35 (K_d = 4.4 nM and 4.5 nM for $A\beta_{1-40}$ and amylin, respectively). This finding clearly indicated the importance of a sufficiently long and hydrophobic spacer (C10) between the chelate and the targeting unit in order to achieve an affinity similar to that of the PiB unit itself.

The influence of GdL31 and GdL34–35 on the $A\beta_{1-40}$ aggregation was investigated using thioflavin-T (Th-T) fluorescence measurements. Th-T is a fluorescent probe with a "turn on" response when it intercalates in β-sheets of amyloid fibrils. According to the orientation of the PiB unit, the Gd^{3+} complexes can either accelerate or slow down the $A\beta_{1-40}$ aggregation process. GdL34 and GdL35 had a higher impact since they were able to delay the peptide aggregation. The decrease in the Th-T fluorescence signal intensity observed in the presence of the complexes indicated a competition for a common binding site. This phenomenon was more obvious for GdL35 and might result from a stronger interaction of the dimethylated aniline part with β-sheets.

Another major conclusion of this work was that the interactions of the Gd^{3+} complexes with the peptide fibrils are concentration-dependent. Indeed, these compounds, composed of a rather hydrophilic metal-coordinating unit and a hydrophobic amyloid-targeting moiety, are amphiphilic. Depending on the concentration and their environment, they tend to form micelle-like aggregates in which the targeting unit can be more or less accessible. The critical micellar concentrations (cmc) from which GdLs form micelles were previously determined for the paramagnetic complexes GdL30–32 (in the 0.5–1.5 mM range) by a relaxometric method, exploiting the change of motional dynamics and thus the relaxation rate between the monomeric and micellar forms. This method was not applicable for GdL34–35 because these complexes are already in a micellar state at lower concentrations. The optical properties of the PiB unit were thus used to measure the cmc of GdL34 and GdL35 (30 and 5 μM, respectively) as well as a pre-micellar concentration for GdL30 and GdL31 (53 and 13 μM, respectively). These data confirmed that different micellization regimes can exist in aqueous solutions depending on GdL concentrations.

These micellization regimes could be then related to the amyloid binding properties of the complexes. Scatchard linearization of the SPR data evidenced different interaction regimes and this was independent of the nature of the peptide (Fig. 3). For each system, these regimes were defined by straight lines with well-defined breakpoints which corresponded well to the cmc or pre-cmc values of the given Gd^{3+} complex as determined above. All these findings seem to indicate that the different aggregated forms of the GdL complexes interact with different affinities with the amyloid peptides.

To characterize their biological behavior, radiolabeled ^{111}InL34 and ^{111}InL35 were injected to wild-type mice. As

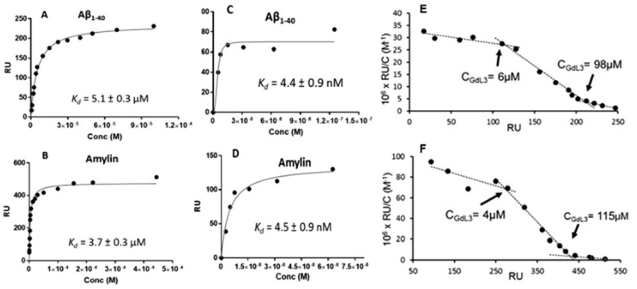

Fig. 3 SPR binding plots fitted as Langmuir isotherm functions for the interaction of GdL35 with $A\beta_{1-40}$ (A and C) and amylin (B and D). Peptide immobilization was 4000 RU (A and B) and 9000 RU (C and D). For C and D, points recorded only at low concentrations are represented. E and F are respectively the Scatchard linearization plots of A and B.

expected, the radiocomplexes had low initial brain uptake, at the same level as that of ^{111}InL30, but fast clearance and no specific organ retention. Nevertheless, the pancreas uptake at 2 min was significant with 2.9% ID per g and 3.7% ID per g, respectively, for ^{111}InL34 and ^{111}InL35. These values are promising for the perspective of amylin imaging, amylin being overexpressed in diabetic animals.

Overall, all these analyses revealed a large complexity of the systems with concentration-dependent binding affinities, which should be always kept in mind when interactions between amphiphilic metal complexes and amyloid peptides are considered.

Probes based on benzofuran derivatives (Table 2)

Benzofuran and benzothiazole are isosteric structures. With respect to benzothiazole, benzofuran has the advantage of easier preparation, since the key step of ring formation can be realized from readily available and less expensive chemicals.[35] It can also be linked to aryl, pyridyl or furanyl groups to enhance amyloid binding properties.

In 2018, Donnelly's group reported new technetium complexes for diagnostic SPECT imaging of cerebral amyloid angiopathy as well as their rhenium analogues (Scheme 6).[36] In the complexes, the metal was coordinated by two pyridylthiosemicarbazide units, which were each conjugated to a functionalized benzofuran group (L36–39). To increase aqueous solubility, for ligands L37 and L39, the methyl substituent in the R2 position was replaced by an *N*,*N*-dimethylaminoethyl functional group.

The interaction with synthetic $A\beta_{1-42}$ was investigated using the well-established Th-T fluorescent probe as a competitor. The rhenium complex $[ReO(HL36)_2]^+$ induced a modest decrease of the Th-T fluorescence signal, considered as not significant, whereas the other complexes produced a reduction of >80%. The most important interaction was observed with $[ReO(HL37)_2]^+$ and $[ReO(HL39)_2]^+$ bearing the *N*,*N*-dimethylaminoethyl group. The authors did not go further with these complexes because the weak benzofuran fluorescence prevented tests on post-mortem brain tissues.

In 2020, the same group reported analogous ligands L40–43 containing the identical pyridyl-benzofuran as a targeting unit and a thiosemicarbazone–pyridylhydrazone structure for copper-64 complexation, thus potential PET application (Scheme 6).[37] The ligand design was inspired by previous work where a styrylpyridyl unit was used for amyloid binding.[38] Here, the choice of a pyridyl benzofuran group was justified by less non-specific binding as compared to styrylpyridine- or benzothiazole-based ligands. Further, to

Table 2 Main properties of benzofuran derivative probes

Ligand number	Molecular weight of ligand	Metal	log *P* of complex	Targeted protein	Affinity to protein[a] (K_i, nM)	Brain uptake at 2 min[b] (% ID per g)	Ref.
36	329.4	Re/^{99m}Tc	—	$A\beta_{1-42}$	—	—	36
37	386.5	Re/^{99m}Tc	—	$A\beta_{1-42}$	—	—	36
38	315.4	Re/^{99m}Tc	—	$A\beta_{1-42}$	—	—	36
39	372.5	Re/^{99m}Tc	—	$A\beta_{1-42}$	—	—	36
40	394.5	^{64}Cu	1.84	$A\beta_{1-42}$	—	1.39	37
41	408.5	^{64}Cu	1.81	$A\beta_{1-42}$	—	1.06	37
42	422.5	^{64}Cu	1.88	$A\beta_{1-42}$	—	0.77	37
43	436.5	^{64}Cu	1.48	$A\beta_{1-42}$	—	1.54	37
44	449.6	^{64}Cu	−0.74	$A\beta_{1-42}$	33.7	0.33/p: 1.66	39
45	623.8	^{64}Cu	−0.73	$A\beta_{1-42}$	243.5	0.36/p: 3.32	39
46	501.5	Re/^{99m}Tc	1.74	Amylin	146	0.08/p: 0.74	41
47	567.7	Re/^{99m}Tc	2.18	Amylin	3430	0.19/p: 1.37	41
48	683.8	^{67}Ga	—	Amylin	3183	0.35/p: 4.11	42
49	572.6	^{64}Cu	−1.02	Aβ	—	—	44
50	600.7	^{64}Cu	−0.37	Aβ	—	—	44
51	628.7	^{64}Cu	0.45	Aβ	—	—	44
52	616.7	^{64}Cu	−0.93	Aβ	—	—	44
53	837.9	^{64}Cu	1.17	Aβ	—	0.65	44
54	894.0	^{64}Cu	1.32	Aβ	—	0.76	44
55	950.1	^{64}Cu	1.77	Aβ	—	0.38	44
56	926.0	^{64}Cu	1.02	Aβ	—	2.34	44

[a] Metal complexes. [b] p = pancreas; AD = murine or rat model of Alzheimer's disease.

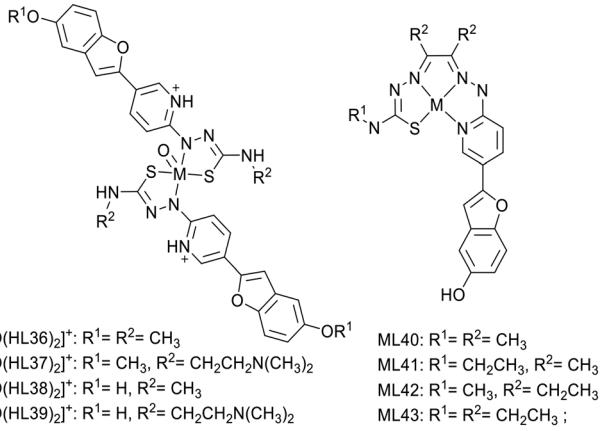

Scheme 6 Pyridyl-benzofuran-derivative technetium complexes reported for diagnostic SPECT imaging of cerebral amyloid angiopathy and copper(II)$^{+}$ complexes containing a coordinating pyridyl-benzofuran unit for PET applications.

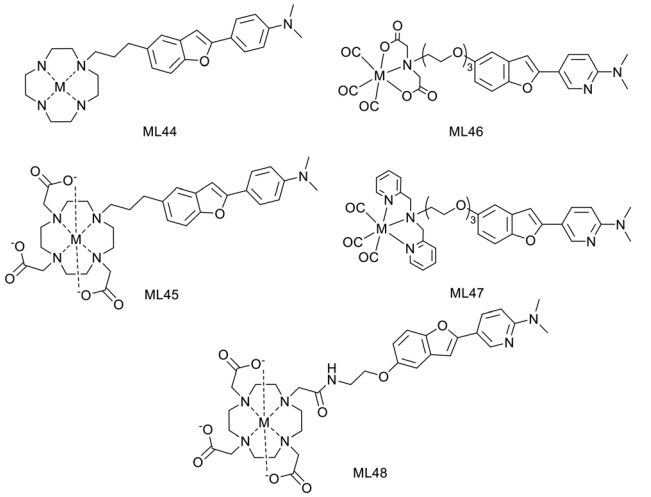

Scheme 7 Metal-based probes containing a phenyl or a pyridyl-benzofuran unit.

minimize the molecular weight, the pyridyl part also serves for metal coordination, and to modulate the *in vivo* behavior and Aβ interactions, methyl or ethyl groups were introduced to the ligand backbone.

The Cu^{2+} complexes were stable with respect to metal dissociation ($K_{d\ (7.4)} \sim 10^{-18}$ M) and resistant to reduction but had different metabolic stabilities. This was tested by incubating the Cu^{2+} complexes with human or murine liver microsomes which contain cytochrome P450, the major enzyme involved in drug metabolism. CuL43, which bears 3 ethyl groups, exhibited the longest half-life, 7–8 times longer than that of CuL40 which has 3 methyl groups (29 *vs.* 4 min in human liver microsomes). CuL41 and CuL42 with 1 or 2 ethyl groups presented intermediate and almost similar stabilities (12 and 11 min half-life, respectively). These results nicely indicated how subtle modifications on the ligand backbone imply metabolic stability alterations of the Cu^{2+} complexes.

All the ^{64}Cu complexes displayed suitable lipophilicity to cross the BBB, and their brain delivery was assessed in wild-type mice. ^{64}CuL40 and ^{64}CuL43 possessed an initial brain uptake of 1.39 and 1.54% ID per g, respectively, but ^{64}CuL43 was more promising because of its faster clearance (2/30 min ratio of 2.0 *vs.* 1.3), which is a required feature in healthy mice without amyloid plaques. Its interaction with synthetic Aβ amyloid peptide was thus studied first by TEM, resulting in a dramatic change in the morphology of the amyloid fibrils. Analysis of *post mortem* human AD brain tissue demonstrated that CuL43 preferentially binds to brain areas identified as being rich in Aβ plaques (measured by immunohistochemistry in the contiguous section of brain tissue).

H. Watanabe and M. Ono have developed 2 macrocyclic ligands where either a cyclen (L44) or a DO3A (L45) is conjugated to a phenylbenzofuran group through a propyl linker (Scheme 7).[39] These macrocycles are known to form stable Cu^{2+} complexes and thus the corresponding $^{64}Cu^{2+}$ chelates have been investigated as PET imaging probes for Aβ fibril detection.

In vitro competitive assays were carried out with the standard radiotracer competitor [^{125}I]IMPY to determine amyloid binding affinities of the cold Cu^{2+} complexes. CuL44 and CuL45 displayed inhibition constants of 33.7 and 243.5 nM, respectively, which were higher than that for other phenylbenzofuran conjugated probes (10.8–24.4 nM) previously reported by the authors or for IMPY itself (14.8 nM).[35,40] The significant difference between the two complexes was related to the bulkier structure of DO3A and to their different charge. While CuL45 is anionic, CuL44 is cationic and had stronger interaction with the anionic Aβ peptide.

Both complexes remained stable in mouse plasma for 1 hour and stained Aβ plaques in brain tissue sections from Tg2576 mice, even if the behavior of CuL44 was closer to that of the Aβ staining dye Th-S. Biodistribution in normal mice revealed a low initial brain uptake at 2 min for both complexes (0.33–0.36% ID per g), which could be due to the steric bulkiness and the hydrophilic nature of the probes (log $P_{oct/water}$ = −0.74 and −0.73). Interestingly, a higher uptake was observed in pancreas, especially for CuL45 (3.32% ID per g), which also exhibited a good clearance. These results suggest that CuL44 and CuL45 do not have the best properties for brain imaging but may be suitable for amylin detection or for cerebral amyloid angiopathy imaging.

H. Watanabe and M. Ono reported three metal-based probes containing a pyridylbenzofuran (PBF) derivative to detect amylin by SPECT imaging. PBF was described to show high affinity for amylin aggregates (Scheme 7). The first report in 2016 proposed two technetium complexes where the pyridylbenzofuran is conjugated, *via* a triethylene glycol linker, to an iminodiacetic acid (IDA, L46) or to *N*,*N*-dipicolylamine (DPA, L47).[41] Later, the same targeting unit was linked to ^{67}GaDO3A through a propylacetamide coordinating spacer (L48).[42]

In vitro competitive inhibition assays were performed with rhenium analogues and the cold Ga^{3+} complex, using the ^{125}I-labeled pyridylbenzofuran derivative [^{125}I]IPBF, which demonstrated high binding affinity for amylin (K_d = 8.3 nM). While ReL46 displayed moderate affinity (K_i = 146 nM), ReL47 and GaL48 presented low affinities (K_i = 3430 and 3183 nM, respectively). The difference between the two rhenium complexes was attributed to their different size and charge. The steric hindrance of the bulkier DPA unit may decrease affinity. IDA forms negatively charged complexes with ^{99m}Tc, while DPA complexes are positively charged.[43] This may also affect the affinity for amylin aggregates since this peptide displays a positive charge. Concerning GaL48, the bulky DOTA linked *via* a short alkyl chain to PBF could cause steric hindrance; a longer linker may improve the amylin binding properties.

In vitro autoradiography on healthy and T2D human pancreas sections confirmed the amylin binding properties of the ^{99m}Tc-labeled probes. ^{99m}TcL46 specifically binds to islet amyloid in T2D pancreatic tissue section, with little nonspecific accumulation, while ^{99m}TcL47 does not show specific binding to amylin. Despite its high inhibition constant, ^{67}GaL48 displayed specific binding to amylin aggregates on T2D pancreas, which was explained by possible differences in the structure of amylin aggregates formed *in vitro* and *in vivo*.

It is important to note that the same authors also developed a novel, easy to prepare and ready to use islet amyloid mouse model in which human amylin aggregates are directly transplanted in the pancreas. *Ex vivo* autoradiography experiments with this model corroborated the poor amylin binding ability of ^{99m}TcL47 and the good labelling potential of ^{99m}TcL46 and ^{67}GaL48. In contrast to the previous *in vitro* experiments, some nonspecific binding was identified for both complexes, suggesting their more important retention in normal tissue in the living pancreas than in tissue sections.

Biodistribution studies in normal mice indicated different pancreatic uptake for ^{99m}TcL46 and ^{67}GaL48. Whereas ^{67}GaL48 presented a high initial uptake but a slow wash-out (4.1% ID per g at 2 min and 2.5% ID per g at 60 min), ^{99m}TcL46 exhibited only 0.74% ID per g at 2 min. The uptake remained significant over 60 min in the pancreas and also in the liver (and in the spleen for ^{67}GaL48). Such nonspecific binding in these organs may make it difficult to visualize pancreatic islet amyloids *in vivo*. ^{99m}TcL46 was also injected in the mouse model with transplanted amylin aggregates. Higher pancreas accumulation of the radiotracer was observed as compared to normal mice (1.6 fold at 1 h post-injection), demonstrating both the binding ability of ^{99m}TcL46 and the value of this model for the validation of amylin imaging probes.

L. M. Mirica published, in 2020, a series of multivalent ligands (L53–L56) containing two new furanyl-hydroxymethylbenzofuran derivatives for copper(II) complexation (Scheme 8).[44] The Aβ-recognition fragment was conjugated to the macrocyclic chelator NOTA *via* four different spacers (ethyl, butyl, hexyl and ethylene glycol). Analogues (L49–L52) with a single targeting unit were also prepared for comparison.

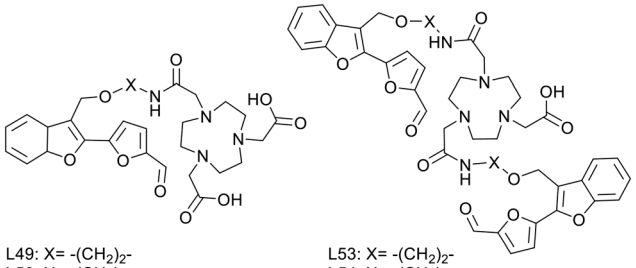

Scheme 8 Furanyl-hydroxymethylbenzofuran derivatives for copper(II) complexation.

Brain section staining from 3-month-old 5xFAD mice with the divalent complexes CuL53–56 showed specific binding to amyloid plaques. CuL54 and CuL55, with butyl and hexyl linkers, exhibited the strongest fluorescence signals and the closest co-localization with the amyloid fibril specific AF594-HJ3.4 antibody. *Ex vivo* data on WT and transgenic mice confirmed specific binding to Aβ plaques and negligible nonspecific interaction with other biomolecules in the brain. ^{64}CuL54 and ^{64}CuL55 led to the highest autoradiography contrast between 5xFAD and WT. In similar experiments, the monovalent ^{64}CuL50 and ^{64}CuL51 analogues yielded 1.5–1.6 lower signal intensities, confirming the existence of a multivalent binding effect.

An additional benefit of the divalent targeting approach was the increased lipophilicity. While $\log P_{oct/PBS}$ ranged between −1.02 and 0.45 for the monovalent complexes, the divalent ones had optimal lipophilicity for potential *in vivo* brain imaging ($\log P_{oct/PBS}$ of 1.02–1.77), which could be finely modulated by the nature and the length of the linker (ethylene glycol ~ ethyl < butyl < hexyl).

In vivo biodistribution of these ^{64}Cu complexes in WT mice showed high initial uptake and fast clearance in each organ. Surprisingly, the most lipophilic ^{64}CuL55 compound had the lowest initial brain uptake and was mostly found in the lungs over 4 hours, whereas ^{64}CuL54 and ^{64}CuL56 had the best BBB permeability and were thus selected for *in vivo* PET imaging with age-matched WT and 5xFAD mice. Post imaging analysis showed a significantly higher brain retention in transgenic *vs.* WT mice for ^{64}CuL54, which thus holds promise as a diagnostic PET imaging agent for AD.

Probes based on stilbene derivatives (Table 3)

Stilbene derivatives are conjugated molecules that were identified to selectively bind Aβ aggregates through hydrophobic non-covalent interactions.

Zhang *et al.* conjugated the previously described Re/^{99m}Tc-chelating BAT group (L12, L13)[26] to styrylpyridine as well *via*

Table 3 Main properties of the stilbene-based probes

Ligand number	Molecular weight of ligand	Metal	log *P* of complex	Targeted protein	Affinity to protein[a] (K_i, nM)	Brain uptake at 2 min[b] (% ID per g)	Ref.
57	490.7	Re/^{99m}Tc	3.04	$A\beta_{1-42}$	13.4	2.10	26
58	534.8	Re/^{99m}Tc	3.15	$A\beta_{1-42}$	142.1	1.10	26
59	327.5	Re/^{99m}Tc	—	$A\beta_{1-42}$	—	—	36
60	384.6	Re/^{99m}Tc	—	$A\beta_{1-42}$	—	—	36
61	463.6	Re	0.39	$A\beta_{1-40}$	—	—	25
62	430.5	^{99m}Tc	1.87	$A\beta_{1-40}$	855	—	45
63	384.5	^{99m}Tc	1.54	$A\beta_{1-40}$	260	0.15	46
64	370.5	^{99m}Tc	2.04	$A\beta_{1-40}$	241	0.36	46
65	356.5	^{99m}Tc	—	$A\beta_{1-40}$	260	—	46
66	453.6	^{64}Cu	1.60	$A\beta_{1-40}$	—	—	47
67	467.7	^{64}Cu	1.61	$A\beta_{1-40}$	—	2.2	47
68	481.7	^{64}Cu	1.50	$A\beta_{1-40}$	—	—	47
69	495.7	^{64}Cu	1.59	$A\beta_{1-40}$	—	—	47
70	495.7	^{64}Cu	1.44	$A\beta_{1-40}$	—	—	47
71	509.7	^{64}Cu	1.56	$A\beta_{1-40}$	—	1.1	47
72	540.8	^{64}Cu	1.03	$A\beta_{1-42}$	—	0.75 AD: 0.79	48

[a] Metal complexes. [b] p = pancreas; AD = murine or rat model of Alzheimer's disease.

one or two oligoethyleneoxy blocks (L57, L58) (Scheme 9). The Re/^{99m}Tc complexes exhibited efficient and specific binding to Aβ plaques in brain, with linker-dependent affinities: the shorter oligoethyleneoxy spacer translated to higher affinity (K_i = 13.4 nM for ^{99m}TcL57 and 102.6 nM for ^{99m}TcL58). The replacement of the 2-arylbenzothiazole scaffold in L12 and L13 with the styrylpyridine led to more favorable initial brain uptake especially for ^{99m}TcL57 (2.10% ID per g at 2 min), while ^{99m}TcL58 showed lower brain delivery (1.10% ID per g at 2 min) and faster clearance (2 min/60 min = 7.33).

^{99m}TcL57, with the best overall properties, was selected for further investigations such as *ex vivo* autoradiography in transgenic/WT age matched mice and *in vivo* SPECT/CT imaging in rhesus monkeys. The good BBB permeability and the specific binding to Aβ plaques in transgenic mouse brain sections was confirmed by the excellent matching with the Th-S stained signal, while no evidence was detected in normal mice. The *in vivo* study in rhesus monkeys showed a significantly improved brain uptake, compared to a previous ^{99m}Tc imaging probe containing an alkyl linker and a benzothiazole unit, studied in the same animals (1.94–2.63% ID *vs.* 0.78–1.23% ID). Since no Aβ amyloid plaques are expected in these monkey's brains, this study did not evaluate the specific binding ability of the probe, but demonstrated its potential use for future human brain imaging.

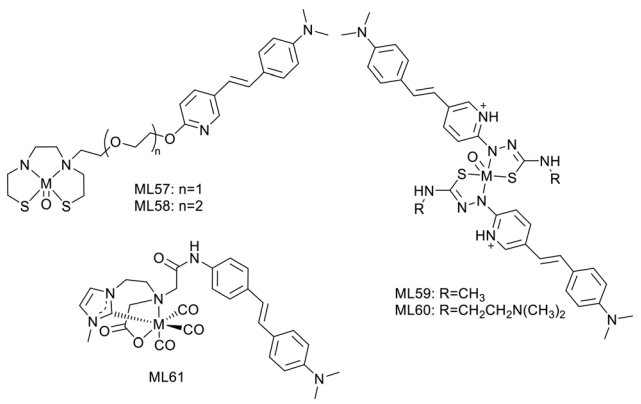

Scheme 9 Stilbene and styrylpiridine derivative ^{99m}Tc complexes.

Other examples of stilbene derivative Re/^{99m}Tc or $^{64}Cu^{2+}$ complexes were described by P. S. Donnelly and co-workers (Scheme 9). As shown above, two substituted pyridylthiocarbazide ligands were coordinated to rhenium,[36] and the authors replaced the benzofuran unit, characterized by insufficient fluorescence properties, with styrylpyridine (L59). An *N*,*N*-dimethylaminoethyl group was also added to increase solubility and modulate the binding properties (L60).

Competitive assays with Th-T in the presence of $A\beta_{1-42}$ aggregates revealed strong reduction of the Th-T fluorescence, suggesting competitive binding or inhibition of fibril formation, especially with $ReO(L60)_2$. The fluorescence of the styrylpyridine group allowed for detecting the complexes in *post mortem* human brain tissue using epi-fluorescence microscopy. Comparison with an Aβ specific antibody (1E8) indicated good co-localization with $Re(L60)_2$, demonstrating significant and specific binding to Aβ plaques. The synthesis of radiolabelled ^{99m}Tc analogues was simple and gave good radiochemical yield, allowing for further investigations towards CAA diagnosis.

Another example by Wiratpruk *et al.* was already discussed in the benzothiazole section.[25] The authors also studied the stilbene-based analogue of the neutral NHC complex ReL61 (Scheme 9). The Th-T competition assay in the presence of $A\beta_{1-40}$ aggregates showed no difference between the benzothiazole and the stilbene derivative complexes. Staining

of human AD brain revealed poor co-localization of ReL61 with the 1E8 antibody, which could be the consequence of the short linker in the structure. Comparison with the age-matched controls did not indicate non-specific binding in brain tissues. The $\log P_{oct/water}$ = 0.39 indicated slightly higher lipophilicity than that of the benzothiazole derivative ReL11 ($\log P_{oct/water}$ = 0.15), but not favourable enough for a good brain delivery.

This group also described, in 2016, a neutral oxorhenium(v) complex ReL62 based on a N_3O tetradentate ligand with a metal-coordinating styrylpyridine group as an Aβ binding moiety (Scheme 10). This complex was identified to specifically bind Aβ plaques in *post mortem* human AD brain tissues[45] and displayed suitable lipophilicity for BBB crossing, but the stability with respect to ligand exchange and radiochemical yield of the technetium analogues had to be improved. Thus, another family of oxorhenium(v) chelates was recently investigated,[46] where the phenolate of ReL62 was replaced with a thiolate donor atom to lead to a N_3S ligand, where the styrylpyridine part is still coordinated to the metal (Scheme 10). The amide functions (0, 1 or 2) in the ligand backbone contribute to increased stability.

Inhibition constants of 240–260 nM were determined for all complexes by competition with Th-T in the presence of synthetic $A\beta_{1-40}$ aggregates. Interaction with amyloid plaques in human brain tissue revealed specific binding outlined by an excellent co-localization with the 1E8 antibody. Further investigations were not possible with ^{99m}TcL65 because of poor radiolabeling, contrary to the other two complexes ^{99m}TcL63–64. It appeared that at least one amide function is necessary for complete radiolabeling with such ligands.

The lipophilic character of these complexes ($\log P_{oct/PBS}$ of 1.54 and 2.04 for ^{99m}TcL63 and ^{99m}TcL64, respectively) might be suitable to cross the BBB. Whereas the substitution of an amide with an amine function significantly increases the lipophilicity, amides are important for complex stability with respect to ligand competition (such as histidine and cysteine).

Biodistribution in wild-type mice indicated the highest brain uptake for the monoamide–monoamine complex but still too low for further SPECT investigations (% ID per g = 0.15 and 0.36 for ^{99m}TcL63 and ^{99m}TcL64, respectively). This low brain delivery may be explained by the hydrogen-bond acceptor character of each amide function towards water molecules, resulting in an extensive hydrogen-bonded array which would reduce BBB permeability.

The authors expect that further structural modifications on the bis(amine) ligand, such as the introduction of geminal methyl substituents on the carbon adjacent to the sulfur donor, will improve the complex stability and the BBB crossing properties.

P. S. Donnelly and co-workers also developed, in 2020, a novel series of six Cu^{2+} complexes, based on bis(thiosemicarbazone) and conjugated to substituted stilbenyl functional groups (ML66–71) (Scheme 11).[47] The authors already used similar bis(thiosemicarbazone) ligands as Cu^{2+} chelators but with benzofuran (*cf.* benzofuran derivatives section) or coordinating styrylpyridine amyloid recognition units and observed low brain delivery. The aim of this present work was thus to improve brain uptake.

The stilbene functional group was directly attached to one thiosemicarbazone limb of the ligand through a stable N^4-substituted thiosemicarbazone functional group. Electron-donating substituents are present on the stilbene unit to favor binding to amyloid aggregates. The ethyl or methyl groups on the ligand backbone are important to modulate lipophilicity, membrane permeability, retention and interaction with serum proteins as well as to retain the redox stability of the Cu^{2+} complexes.

The stability of the Cu^{2+} complexes was confirmed with respect to reduction and decomplexation in the presence of a large excess of glutathione, the most abundant biological reductant and copper binding ligand. The alkyl substituents on the ligand backbone did not induce significant changes in the distribution coefficient. Indeed, all the ^{64}Cu complexes presented a similar lipophilic character with $\log P_{oct/PBS}$ = 1.44–1.61, which might be appropriate for brain delivery.

Competition assays with Th-T in the presence of $A\beta_{1-40}$ revealed reduced ThT fluorescence upon addition of all CuL66–71 complexes, indicative of competitive binding or inhibition of Aβ fibril formation. As all complexes had similar properties, the authors arbitrarily chose two compounds for supplementary studies: CuL67 and CuL71, with the lowest and the highest molecular weight, respectively. They both showed specific binding to Aβ plaques

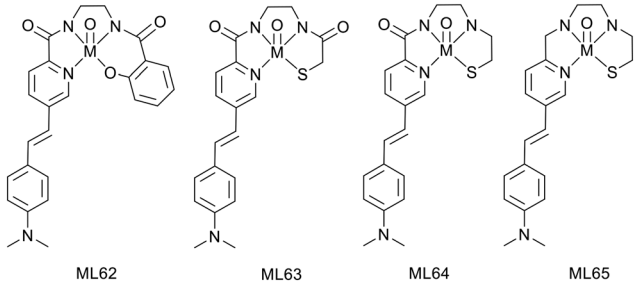

Scheme 10 ^{99m}Tc complexes with metal-coordinating styrylpyridine moiety.

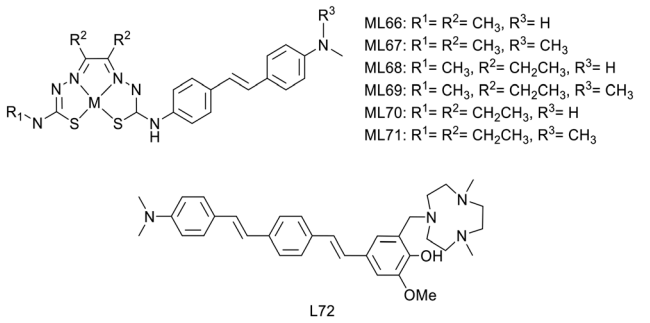

Scheme 11 Stilbene and distyrylbenzene derivatives for copper(II) complexation.

on *post mortem* human brain sections from confirmed AD patients as well as nonspecific binding on healthy tissues from age-matched control subjects.

^{64}CuL67 and ^{64}CuL71 crossed the BBB in wild-type mice, with initial brain uptake of 2.2 and 1.1% ID per g, respectively. These levels were similar to that of ^{64}Cu(ATSM) already used in humans and better than that of another previously reported Cu^{2+}-thiosemicarbazone–styrylpyridylhydrazone complex.[38] Future investigations are envisaged in transgenic murine models of amyloid pathologies, and this work could also be adapted to other radioisotopes of copper such as ^{60}Cu, ^{61}Cu or ^{62}Cu for imaging.

Recently, L. M. Mirica's group developed compound L72 by linking the hydrophilic triazamacrocycle (Me_2TACN) to a hydrophobic distyrylbenzene derivative through a 2-methoxyphenol fragment (Scheme 11), which is known to display antioxidant properties and to inhibit the formation of Aβ fibrils.[48] Most of this work focused on the ligand itself, in terms of interaction with $Aβ_{1–42}$ oligomers and aggregates, a fluorescence turn-on effect, *in vivo* BBB penetration and therapeutic potential. However, the authors also used the copper chelating properties of azamacrocycle and investigated the PET tracer ^{64}CuL72. The ligand is monocationic since one amine of the macrocycle is protonated, and it is expected that the Cu^{2+} complex possesses the same charge due to the deprotonation of the phenolate group. Thus, both the ligand and the Cu^{2+} complex displayed similar turn-on fluorescence in the presence of $Aβ_{1–42}$ oligomers and fibrils. *Ex vivo* fluorescence staining on brain sections of 7 month old 5xFAD transgenic mice indicated selective binding of CuL72 to Aβ species (fibrils and oligomers). Indeed, good co-localization has been observed with Congo red and HJ3.4 and OMAB antibodies which respectively bind to a large range of Aβ species and specifically to Aβ oligomers. *Ex vivo* autoradiography comparison between 10 month old 5xFAD and WT mouse brain sections further confirmed specific binding of ^{64}CuL72 to Aβ species. The authors concluded that an amphiphilic molecule containing a hydrophilic fragment attached to a hydrophobic amyloid targeting unit is suitable to attain good binding affinity for both soluble and insoluble Aβ aggregates.

Finally, the pharmacokinetics of ^{64}CuL72 was explored in 5xFAD and age-matched WT mice, and revealed BBB permeability and brain accumulation in AD mice. Normal and transgenic animals exhibited quite similar initial brain uptake (0.75% ID per g *vs.* 0.79% ID per g), but the wash-out was rapid in WT mice, in contrast to more important brain retention in the 5xFAD model.

Probes based on other small amyloid recognition moieties (Table 4)

Following their previous work on ^{18}F fluorinated phenylquinoxaline moiety for tau targeting,[49] Yang *et al.* explored a set of complexes based on phenylquinoxaline functionalized with a diethyl iminodiacetate group for the coordination of ^{99m}Tc and Re (ML73–76).[50] The complexes varied in the position of the *N*,*N*-dimethyl amino group and in the size of the linker between the chelator and the targeting unit (Scheme 12). Variation of the position of the methyl group yielded selectivity of these probes for tau *vs.* Aβ, as indicated by their different affinities to those proteins.

Indeed, K_d values ranging from 60 nM to 3.4 μM were obtained, and the ratio between the affinity to the two proteins for a given complex was 10 to 20. To further evaluate the potential of ^{99m}TcL74 and ^{99m}TcL76, *ex vivo* studies were performed in normal mice. The initial brain uptake for ^{99m}TcL74 (0.61% ID per g, $\log D$ = 2.11), although not striking, was higher than that for ^{99m} TcL76 (0.34% ID per g, $\log P_{oct/PBS}$ = 1.43), probably due to the additional carbon in the linker and the subsequently increased lipophilicity of ^{99m}TcL74. A clearance ratio 2/60 min of 3.2 and 3.8 was found for ^{99m}TcL74 and ^{99m}TcL76 complexes, respectively. Moreover, brain slices from human AD patients and from Tg-tau AD mice were stained with the ReL74 analogue and its tau targeting ability was validated by Gallyas–Braak staining (which detects phosphorylated tau accumulation). Overall, ^{99m}TcL74 exhibited high and selective binding ability to neurofibrillary tangles, composed of hyperphosphorylated tau, but more structure optimizations should be performed to further improve the BBB permeability.

Tryptamine, an indole derivative, was also explored as a targeting moiety. Rastogi *et al.* proposed a Mn^{2+} complex functionalized with tryptamine as a potential T_1/T_2 contrast agent.[51] The Mn^{2+} ion is 7-coordinated by the ligands (precursor MnL77 and tryptamine derivative MnL78) and the complexes hold one water molecule in their inner sphere, as confirmed by the solid-state structures (Scheme 13).

The presence of the water molecule yielded surprisingly high relaxivities, r_1 = 6.74 to 7.26 mM^{-1} s^{-1} and r_2 = 33.38 to 23.26 mM^{-1} s^{-1} at 7 T for MnL77 and MnL78, respectively. The differences between the two chelates have been attributed to the increase in both the molecular weight and the rigidity of the complex upon tryptamine functionalization. Affinity studies towards Aβ-fibrils showed a K_d of 3.19 μM for MnL78, while MnL80 did not interact with Aβ-fibrils, highlighting the targeting properties of the indole group.

Chalcone was widely explored as a scaffold for medicinal applications. Chalcone analogues were used as inhibitors of enzymes or proteins involved in the pathogenesis of AD as well as a targeting moiety for imaging.[52] A recent chalcone-based MRI probe was reported by Choi *et al.*[53] The GdL79 complex consists of a DO3A bearing a chalcone unit functionalised with a dimethylamino group (Scheme 14). The latter is expected to improve Aβ binding as well as the fluorescence properties of the targeting moiety, enabling optical imaging. The probe had a $\log P_{oct/water}$ of −0.32 and K_d of 23.1 μM, thus an 8-fold higher binding affinity to Aβ aggregates than the non-targeted agent Gadobutrol®.

Table 4 Main properties of the other small amyloid recognition, peptide and antibody moieties

Ligand number	Molecular weight of ligand	Metal	log *P* of complex	Targeted protein	Affinity to protein[a] (K_i, nM)	Brain uptake at 2 min[b] (% ID per g)	Ref.
73	452.5	Re/^{99m}Tc	1.69	$A\beta_{1-42}$	1920	—	50
74	452.5	Re/^{99m}Tc	2.11	$A\beta_{1-42}$	1214	0.61/p: 2.59	50
75	438.5	Re/^{99m}Tc	1.17	$A\beta_{1-42}$	3422	—	50
76	438.5	Re/^{99m}Tc	1.43	$A\beta_{1-42}$	1475	0.34/p: 1.93	50
77	497.6	Mn	—	Aβ	—	—	51
78	683.8	Mn	—	Aβ	3190	—	51
79	652.8	Gd	−0.32	$A\beta_{1-42}$	$2.31 \times 10^{4\$}$	—	53
80	448.5	^{99m}Tc	1.08	$A\beta_{1-42}$	$33.2^{\S}$	0.78	54
81	462.5	^{99m}Tc	1.1	$A\beta_{1-42}$	$102.5^{\S}$	0.86	54
82	959	Gd	—	$A\beta_{1-40}$/$A\beta_{1-42}$	1–40: $9 \times 10^{4\$}$ 1–42: $3 \times 10^{5\$}$	—	55
83	1170	^{99m}Tc	1.6	Aβ	$20.22^{\$}$	0.35 AD: 0.38	56
84	145 000	^{89}Zr	—	Aβ	$0.85^{\$}$	—	58
85	15 700	Gd	—	Aβ	$19^{\S}$	—	59

[a] Metal complexes; $^{\$}K_d$; $^{\S}IC_{50}$. [b] p = pancreas; AD = murine or rat model of Alzheimer's disease.

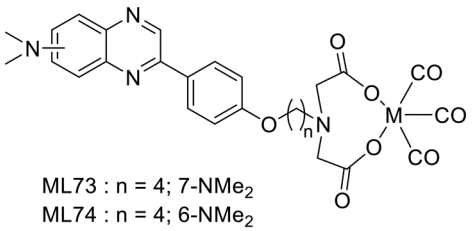

Scheme 12 Phenylquinoxaline derivative ^{99m}Tc complexes.

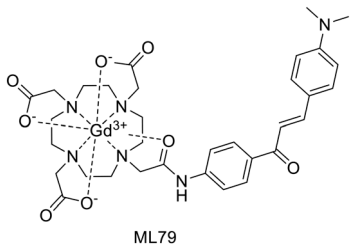

Scheme 14 Chalcone derivative Gd^{3+} complex.

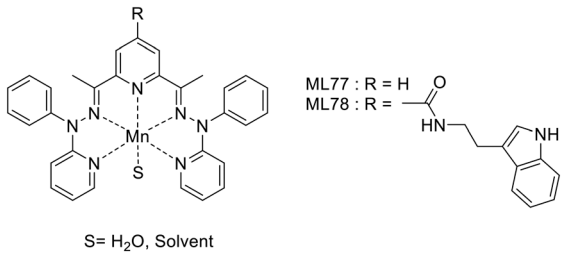

Scheme 13 Tryptamine derivative Mn^{2+} complexes.

The relaxivities of GdL79, r_1 = 4.95 and r_2 = 6.80 mM^{-1} s^{-1} at 3 T and r_1 = 4.99 and r_2 = 6.07 mM^{-1} s^{-1} at 9.4 T, were superior to those of the gold standard MRI contrast agent Gd(DOTA) and Gadobutrol®. An MRI phantom study was performed at 9.4 T to highlight the binding to Aβ and the potential of this probe for the MRI detection of low- (di-, tri-, tetramer) and high-molecular-weight (75–250 kDa) Aβ oligomers. A significant increase in MR signal intensity was observed when GdL79 was incubated with high-molecular-weight Aβ oligomers. These promising results led the authors to explore this probe *in vivo*, in 5XFAD transgenic mice upon IV administration of GdL79 at a dose of 0.3 mmol kg^{-1}. Thanks to the good lipophilicity and Aβ affinity of this complex, the MR images at 4 h post injection showed signal enhancement in the brain in Aβ-containing areas which were confirmed in matched histological sections (Fig. 4).

Molavipordanjani *et al.* conceived a set of 6 2-aryl-imidazo[2,1-*b*]benzothiazole (IBT) derivatives (Scheme 15).[54] The IBT scaffold combines the benzothiazole part of PiB and the 2-arylimidazo part of IMPY. This lipophilic, planar and electron-rich conjugated heteroaromatic system is expected to improve BBB crossing and thus enable *in vivo* imaging of AD brains. For ^{99m}Tc radiolabelling, IBT was conjugated with 3 different units: (i) 2-thiophenemethylamine, (ii) picolylamine or (iii) ethyl glycinate, *via* a linker of two or three carbons. Only the latter displayed proper ^{99m}Tc labelling features (ML80–81); therefore further studies were restricted to these two complexes.

Both radiocomplexes showed a lipophilic nature ($\log P_{oct/water}$ = 1.08 and 1.10 for ^{99m}TcL80 and ^{99m}TcL81, respectively) and competition binding assays revealed that ^{99m}TcL81 has a 3.8-fold higher affinity towards $A\beta_{1-42}$, with IC_{50} values of 33.2 and 102.5 nM. Biodistribution studies in normal mice yielded initial brain uptake at 2 min post-injection of 0.78 and 0.86% ID per g for ^{99m}TcL80 and ^{99m}TcL81, respectively. The brain clearance ratios 2 to 60 min (8.67 and 7.17, respectively) indicated a good *in vivo* profile. The radiocomplexes were mainly eliminated *via* the hepatobiliary route, resulting in high radioactivity in the liver and intestines. Autoradiography was performed on brain

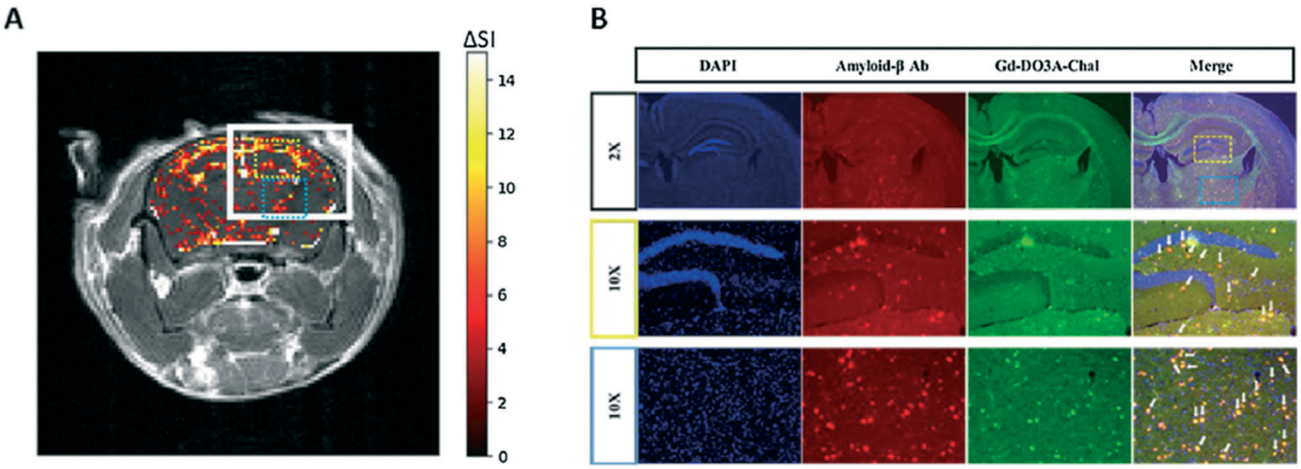

Fig. 4 (A) Color mapped T_1-weighted MR image of brain AD mouse model 4 h after intravenous administration of GdL79; (B) *post mortem* immunofluorescence imaging after MR acquisition, showing co-localization of GdL79 (green) and amyloid beta antibody (red). Reprinted from ref. 53. Copyright 2020 with permission from Elsevier.

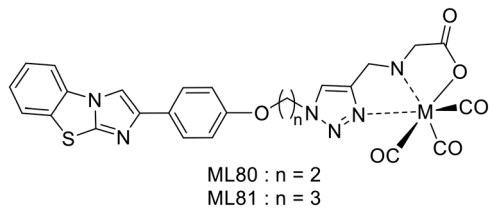

Scheme 15 2-Aryl-imidazo[2,1-*b*]benzothiazole (IBT) derivative ^{99m}Tc complexes.

sections of the AD rat model. ^{99m}TcL80 and ^{99m}TcL81 did not accumulate in control slices, while a hot spot was observed for both at the area of Aβ plaques and their co-localization was confirmed by Congo red staining experiments.

BBB-permeable and Aβ-targeted dyads obtained by conjugation of Gd(DOTA) to carbazole-based cyanine were recently reported.[55] The complex GdL82 (Scheme 16) exhibited a relaxivity of 4.42 mM^{-1} s^{-1} at 3 T. The cyanine moiety could inhibit self-aggregation of Aβ, as shown by the ThT fluorescence assay, with an IC_{50} value of 2.83 μM. *In vivo* T_1-weighted images (with 10 mg kg^{-1} injected dose, at 7 T) of 6 month-old 2xTg-AD mice led to brighter images, at different depths of the brain, at 90 min post injection than before injection, in sharp contrast to those from age-matched WT mice, demonstrating the capability of this complex to serve as an effective and sensitive T_1-weighted MRI contrast agent for cerebral Aβ imaging *in vivo*.

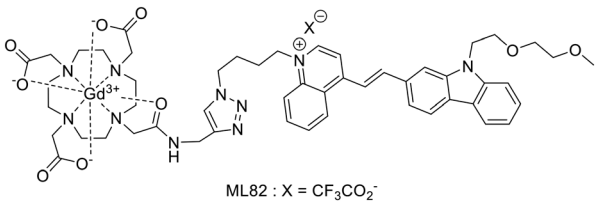

Scheme 16 Gd(DOTA) conjugated to carbazole-based cyanine.

Probes based on peptide or antibody moieties (Table 4)

To specifically target the fibril ends of $Aβ_{1–42}$ deposits, LPFFD and KLVFF, two pentapeptides known to bind to Aβ, were selected and grafted on small gadolinium-based AGuIX nanoparticles modified by a PEG chain.[32] The resulting nanoparticles AGuIX@PEG@LPFFD and AGuIX@PEG@KLVFF are ≈3 nm in diameter and display r_1 relaxivities of 13.2 and 14.1 mM^{-1} s^{-1} and r_2 of 20.1 and 23.0 mM^{-1} s^{-1} (at 60 MHz and 37 °C), respectively. Extra functionalisation with the fluorophore Cy5.5 was performed to enable the determination of the affinity of these particles towards $Aβ_{1–42}$. Surprisingly, no binding has been detected under the conditions studied, while SPR measurements yielded K_d of 534 μM for AGuIX@PEG@KLVFF@Cy5.5 and of 261 μM for AGuIX@PEG@LPFFD@Cy5.5. Cytotoxicity studies showed good tolerance of the cells even for Gd^{3+} concentrations as high as 5 mM. Finally, incubation of these particles with AD mouse brain slices revealed their co-localization with Aβ plaques.

Another probe consisted of a small lipophilic peptide (FPLIAIMA) previously reported to bind to Aβ, and a cyclopentadienyl tricarbonyl ^{99m}Tc complex.[56] ^{99m}Tc-Cp-GABA-D-(FPLIAIMA)-NH_2 (^{99m}TcL83, Scheme 17) displayed log $P_{oct/PBS}$ = 1.6 and K_d = 20 μM towards $Aβ_{1–42}$. *In vivo* studies in control and AD model rats revealed moderate initial brain uptake (0.38 and 0.35% ID per g, respectively, at 2 min post-injection). Notably, AD rats showed a high retention in the brain at 30 min (0.23% ID per g) in comparison with fast clearance in normal rat brains.

Specific antibodies are well-known targeting moieties and have the advantage of conferring a high affinity to the imaging probes. Nevertheless, their slow pharmacokinetics is not well adapted to all imaging techniques.[57] Only long-lived isotopes are appropriate for the design of antibody-based imaging

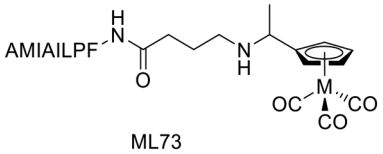

Scheme 17 Aβ targeting with a small lipophilic peptide conjugated to a $[Cp^{99m}Tc(CO)_3]$ unit.

probes. It is the case of ^{89}Zr, with a half-life of 78.4 h, *vs.* short half-lives of currently used isotopes such as ^{18}F (111 min), ^{99m}Tc (6 h) or ^{64}Cu (12.7 h). The monoclonal antibody JRF/AβN/25 directed against the full-length human $Aβ_{1–x}$ epitope was conjugated to a Df-Bz-NCS chelator.[58] ^{89}Zr-Df-Bz-JRF/AβN/25 (ML84; Scheme 18) conserved its nanomolar affinity to $Aβ_{1–40}$ (K_d = 0.85 nM) and biodistribution studies in healthy WT mice showed an accumulation of 0.5 and 0.36% ID per g at 1 h and 48 h post injection, respectively. This uptake was confirmed by *ex vivo* autoradiography performed in mice brain slices.

Camelid single-domain antibody fragments (VHHs), or nanobodies, are smaller (≈15 kDa), stable and highly specific. Vandesquille *et al.* proposed an anti-Aβ VHH, R3VQ, which was conjugated to 2 to 5 Gd(DOTA) units *via* an amide or a thiol bond.[59] DOTA conjugation did not affect $Aβ_{1–40}$ recognition, as all probes displayed IC_{50} in the 19–50 nM range. The potential MRI probe R_3VQ-S-$(Gd(DOTA))_3$ (ML85; Scheme 19) has an r_1 of 19.2 mM^{-1} s^{-1} at 11.7 T (25 °C). Incubation of cerebral hemispheres of PS2APP mouse brains yielded a 7-fold MRI signal intensity difference between spots with amyloid plaques and the baseline and a 33-fold difference with respect to the corresponding hemisphere from WT mice. The presence of Aβ plaques in the AD model brain slices was confirmed by immunohistochemistry.

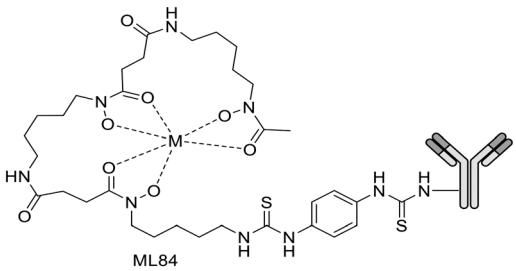

Scheme 18 Monoclonal antibody JRF/AβN/25 conjugated to a Df-Bz-NCS chelator for ^{89}Zr complexation.

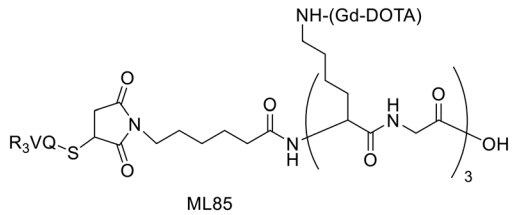

Scheme 19 Anti-Aβ nanobody R3VQ conjugated to Gd(DOTA) units.

Conclusions and perspectives

The development of metal-based probes for imaging detection of amyloid peptides has been a very active field in the past six years. However, despite the high number of amyloid peptides implicated in different pathologies, the large majority of the examples concerns the detection of Aβ fibrils in Alzheimer's disease. The success of such approaches is largely dependent on BBB permeability which remains a very important limitation. Despite the easier accessibility of the target amyloids, only a few studies have been interested so far in imaging Aβ deposits in the context of cerebral amyloid angiopathy or amylin in diabetes. Overall, most reports describe radiocomplexes, mainly with ^{99m}Tc, ^{64}Cu, or ^{68}Ga, for nuclear imaging applications; examples of MRI agents are very scarce. This is not surprising and is obviously related to the much lower sensitivity of MRI which makes MRI detection especially challenging in the brain.

Despite the high number of novel systems investigated in recent years, the chemical versatility of the complexes, and in particular of the amyloid targeting moieties used, remains relatively limited. These are essentially restricted to a few basic structures, mainly derived from benzothiazole, benzofuran or stilbene, while targeting with biological ligands, such as peptides, antibodies or nanobodies, is rather rare. By comparing data on the various small-molecular targeting functions, none of these seems to really emerge in terms of amyloid Aβ binding affinity or promotion of BBB crossing. *In vitro* binding affinity to the fibrils, as mostly assessed by competition assays using radioactive or fluorescent competitors, is typically (slightly) reduced by the presence of the metal chelate, but this influence is governed to a large extent by the length and the chemical nature of the spacer between the chelate and the amyloid recognition moiety. Depending also on the peptide's charge, the charge of the chelate becomes also important, though complete and systematic studies are still lacking. A few divalent probes have been investigated as well; however, these first data are not fully conclusive on a clear benefit of two targeting units for amyloid recognition. Finally, the concentration-dependent aggregation state of the amphiphilic complex itself is also a very important element that affects the amyloid-binding affinity. Such micellization processes are likely non-existing in the concentration range where nuclear imaging probes are used, but they clearly prevail at MRI-related concentrations (from a few μM to mM range).

While it is now standard to evaluate amyloid binding of the probes on tissue, in particular brain sections, originating from pathological mouse models as well as from *post mortem* human patients, an increasingly higher number of *in vivo* data also become available. These do not always confirm the *ex vivo* findings, highlighting the complexity of real biological conditions.

Today, very few comparative data exist on binding constants with different amyloid peptides, and these do not show real selectivity for any of the targeting units

investigated. Selectivity will likely become interesting in the future to distinguish between different fibrils, especially knowing that co-localization of amylin and Aβ has been reported and is thought to be responsible for the cross-talk between diabetes and Alzheimer's disease. In addition, affinity of the probes to other abundant proteins can also be important as it influences their biological fate. This aspect is generally overlooked today but should receive more attention in the future. Potential binding to serum albumin is essential for blood retention, and interaction with other proteins can be responsible for non-specific staining often detected in *ex vivo* experiments.

As for BBB permeability, the common relationships between molecular structure and brain delivery are also validated for metal complexes: smaller size and amphiphilic character promote brain delivery. Structural elements important for amyloid binding, like long and hydrophobic spacers, can also contribute to more adapted lipophilicity, but they also increase the size, which in turn can be detrimental for BBB crossing. Interestingly, several examples exist where one donor atom from the targeting moiety also participates in metal binding in order to limit molecular size, and this does not seem to severely reduce amyloid recognition.

Beyond these general trends, many examples show that even small structural modifications on the ligand can have dramatic consequences on the amyloid-binding properties or the biodistribution of the metal chelates which makes it difficult to fully predict their behaviour.

Future efforts will be increasingly focusing on *in vivo* translation of the imaging agents, and in this respect, pathologies which do not concern the brain are expected to experience more success. In the choice of the biomarker, extracellular localization of the fibrils is also important to facilitate target accessibility. The availability of appropriate preclinical animal models will be a key issue for successful assessment of the novel probes on pathologies other than Alzheimer's disease.

Finally, we should also note that while imaging amyloid plaques remains an important objective, there is increasing evidence that mature fibrillary species might be less relevant than oligomers to assess the severity of the pathology. In AD, soluble Aβ oligomers are accepted today to be more neurotoxic than fibrillary Aβ species and responsible for memory failure, and oligomer levels correlate better with disease progression.[60]

Conflicts of interest

There are no conflicts to declare.

Acknowledgements

The authors acknowledge financial support from the French National Research Agency (ANR-16-CE18-0022). CFGCG thanks the Portuguese Foundation for Science and Technology (FCT)/MCTES for funding the Coimbra Chemistry Centre through the programmes UIDB/00313/2020 and UIDP/00313/2020, also cofunded by FEDER/COMPETE 2020-EU.

Notes and references

1 F. Chiti and C. M. Dobson, *Annu. Rev. Biochem.*, 2017, **86**, 27.
2 C. Giacomelli, S. Daniele and C. Martini, *Biochem. Pharmacol.*, 2017, **131**, 1; D. Eisenberg and M. Jucker, *Cell*, 2012, **148**, 1188.
3 L. Gremer, D. Schölzel, C. Schenk, E. Reinartz, J. Labahn, R. B. G. Ravelli, M. Tusche, C. Lopez-Iglesias, W. Hoyer, H. Heise, D. Willbold and G. F. Schröder, *Science*, 2017, **358**, 116.
4 L. Gatti, F. Tinelli, E. Scelzo, F. Arioli, G. Di Fede, L. Obici, L. Pantoni, G. Giaccone, P. Caroppo, E. A. Parati and A. Bersano, *Int. J. Mol. Sci.*, 2020, **21**, 3435.
5 M. Press, T. Jung, J. König, T. Grune and A. Höhn, *Mech. Ageing Dev.*, 2019, **177**, 46.
6 S. Muralidar, S. V. Ambi, S. Sekaran, D. Thirumalai and B. Palaniappan, *Int. J. Biol. Macromol.*, 2020, **163**, 1599.
7 C. R. Fields, N. Bengoa-Vergniory and R. Wade-Martins, *Front. Mol. Neurosci.*, 2019, **12**, 299.
8 O. Pansarasa, M. Bordoni, L. Diamanti, D. Sproviero, S. Gagliardi and C. Cereda, *Int. J. Mol. Sci.*, 2018, **19**, 1345.
9 D. Chhangani, A. Martín-Peña and D. E. Rincon-Limas, *iScience*, 2021, **24**, 102459.
10 C. P. Argyropoulos, S. S. Chen, Y. H. Ng, M. E. Roumelioti, K. Shaffi, P. P. Singh and A. H. Tzamaloukas, *Front. Med.*, 2017, **4**, 73.
11 X. Wang, X. Wang and Z. Guo, *Coord. Chem. Rev.*, 2018, **362**, 72.
12 P. A. Broderick, L. Wenning and Y. S. Li, *J. Neural Transm.*, 2017, **124**, 57.
13 U. Saeed, J. Compagnone, R. I. Aviv, A. P. Strafella, S. E. Black, A. E. Lang and M. Masellis, *Transl. Neurodegener.*, 2017, **6**, 1.
14 N. J. Cobb and W. K. Surewicz, *Biochemistry*, 2009, **48**, 2574; L.-Q. Wang, K. Zhao, H.-Y. Yuan, Q. Wang, Z. Guan, J. Tao, X.-N. Li, Y. Sun, C.-W. Yi, J. Chen, D. Li, D. Zhang, P. Yin, C. Liu and Y. Liang, *Nat. Struct. Mol. Biol.*, 2020, **27**, 598.
15 D. Adams, H. Koike, M. Slama and T. Coelho, *Nat. Rev. Neurol.*, 2019, **15**, 387.
16 B. R. Smith and S. S. Gambhir, *Chem. Rev.*, 2017, **117**, 901.
17 M. L. James and S. S. Gambhir, *Physiol. Rev.*, 2012, **92**, 897; D.-E. Lee, H. Koo, I.-C. Sun, J. H. Ryu, K. Kim and I. C. Kwon, *Chem. Soc. Rev.*, 2012, **41**, 2656; S. Y. Lee, S. I. Jeon, S. Jung, I. J. Chung and C. H. Ahn, *Adv. Drug Delivery Rev.*, 2014, **76**, 60.
18 R. Weissleder and M. J. Pittet, *Nature*, 2008, **452**, 580.
19 S. Lacerda, J. F. Morfin, C. F. G. C. Geraldes and É. Tóth, *Dalton Trans.*, 2017, **46**, 14461.
20 B. C. Uzuegbunam, D. Librizzi and B. Hooshyar Yousefi, *Molecules*, 2020, **25**, 977.
21 O. Krasnovskaya, D. Spector, A. Zlobin, K. Pavlov, P. Gorelkin, A. Erofeev, E. Beloglazkina and A. Majouga, *Int. J. Mol. Sci.*, 2020, **21**, 9190; K. Chen and M. Cui, *Med. Chem. Commun.*, 2017, **8**, 1393.

22 J. Jia, K. Zhou, J. Dai, B. Liu and M. Cui, *Eur. J. Med. Chem.*, 2016, **124**, 763.
23 C. Kiritsis, B. Mavroidi, A. Shegani, L. Palamaris, G. Loudos, M. Sagnou, I. Pirmettis, M. Papadopoulos and M. Pelecanou, *ACS Med. Chem. Lett.*, 2017, **8**, 1089.
24 M. Sagnou, B. Mavroidi, A. Shegani, M. Paravatou-Petsotas, C. Raptopoulou, V. Psycharis, I. Pirmettis, M. S. Papadopoulos and M. Pelecanou, *J. Med. Chem.*, 2019, **62**, 2638.
25 N. Wiratpruk, A. Noor, C. A. McLean, P. S. Donnelly and P. J. Barnard, *Dalton Trans.*, 2020, **49**, 4559.
26 X. Zhang, Y. Hou, C. Peng, C. Wang, X. Wang, Z. Liang, J. Lu, B. Chen, J. Dai, B. Liu and M. Cui, *J. Med. Chem.*, 2018, **61**, 1330.
27 B. W. Chow and C. Gu, *Trends Neurosci.*, 2015, **38**, 598; C. Y. Chan, A. Noor, C. A. McLean, P. S. Donnelly and P. J. Barnard, *Chem. Commun.*, 2017, **53**, 2311.
28 N. Bandara, A. K. Sharma, S. Krieger, J. W. Schultz, B. H. Han, B. E. Rogers and L. M. Mirica, *J. Am. Chem. Soc.*, 2017, **139**, 12550.
29 Y. Huang, H.-J. Cho, N. Bandara, L. Sun, D. Tran, B. E. Rogers and L. M. Mirica, *Chem. Sci.*, 2020, **11**, 7789.
30 Y. Wang, T. T. Huynh, H.-J. Cho, Y.-C. Wang, B. E. Rogers and L. M. Mirica, *Inorg. Chem.*, 2021, **60**, 12610.
31 A. F. Martins, J.-F. Morfin, A. Kubíčková, V. Kubíček, F. Buron, F. Suzenet, M. Salerno, A. N. Lazar, C. Duyckaerts, N. Arlicot, D. Guilloteau, C. F. G. C. Geraldes and É. Tóth, *ACS Med. Chem. Lett.*, 2013, **4**, 436; A. F. Martins, J.-F. Morfin, C. F. G. C. Geraldes and Éva Tóth, *J. Biol. Inorg. Chem.*, 2014, **19**, 281; A. F. Martins, D. M. Dias, J. F. Morfin, S. Lacerda, D. V. Laurents, É. Tóth and C. F. G. C. Geraldes, *Chem. – Eur. J.*, 2015, **21**, 5413; D. Cressier, M. Dhilly, T. T. Cao Pham, F. Fillesoye, F. Gourand, A. Maïza, A. F. Martins, J.-F. Morfin, C. F. G. C. Geraldes, É. Tóth and L. Barré, *Mol. Imaging Biol.*, 2016, **18**, 334; A. C. Oliveira, T. Costa, L. L. G. Justino, R. Fausto, J.-F. Morfin, É. Tóth, C. F. G. C. Geraldes and H. D. Burrows, *Photochem. Photobiol. Sci.*, 2020, **19**, 1522.
32 M. Plissonneau, J. Pansieri, L. Heinrich-Balard, J.-F. Morfin, N. Stransky-Heilkron, P. Rivory, P. Mowat, M. Dumoulin, R. Cohen, É. Allémann, É. Tóth, M. J. Saraiva, C. Louis, O. Tillement, V. Forge, F. Lux and C. Marquette, *J. Nanobiotechnol.*, 2016, **14**, 60.
33 P. M. Costa, J. T.-W. Wang, J.-F. Morfin, T. Khanum, W. To, J. Sosabowski, E. Tóth and K. T. Al-Jamal, *NANO*, 2018, **2**, 168.
34 S. Majdoub, Z. Garda, A. C. Oliveira, I. Relich, A. Pallier, S. Lacerda, C. Hureau, C. F. G. C. Geraldes, J.-F. Morfin and É. Tóth, *Chem. – Eur. J.*, 2021, **27**, 2009.
35 M. Ono, Y. Fuchi, T. Fuchigami, N. Kobashi, H. Kimura, M. Haratake, H. Saji, M. Nakayama and ACS Med, *Chem. Lett.*, 2010, **1**, 443.
36 S. P. Fletcher, A. Noor, J. L. Hickey, C. A. McLean, J. M. White and P. S. Donnelly, *J. Biol. Inorg. Chem.*, 2018, **23**, 1139.
37 L. E. McInnes, A. Noor, K. Kysenius, C. Cullinane, P. Roselt, C. A. McLean, F. C. K. Chiu, A. K. Powell, P. J. Crouch, J. M. White and P. S. Donnelly, *Inorg. Chem.*, 2019, **58**, 3382.
38 J. L. Hickey, S. Lim, D. J. Hayne, B. M. Paterson, J. M. White, V. L. Villemagne, P. Roselt, D. Binns, C. Cullinane, C. M. Jeffery, R. I. Price, K. J. Barnham and P. S. Donnelly, *J. Am. Chem. Soc.*, 2013, **135**, 16120.
39 H. Watanabe, A. Kawasaki, K. Sano, M. Ono and H. Saji, *Bioorg. Med. Chem.*, 2016, **24**, 3618.
40 H. Watanabe, M. Ono, S. Iikuni, M. Yoshimura, K. Matsumura, H. Kimura and H. Saji, *Bioorg. Med. Chem. Lett.*, 2014, **24**, 4834.
41 M. Yoshimura, M. Ono, H. Watanabe, H. Kimura and H. Saji, *Bioconjugate Chem.*, 2016, **27**, 1532.
42 H. Watanabe, K. Kawano, S. Iikuni, Y. Shimizu and M. Ono, *Nucl. Med. Biol.*, 2020, **90-91**, 93.
43 N. Harada, H. Kimura, M. Ono, D. Mori, Y. Ohmomo, T. Kajimoto, H. Kawashima and H. Saji, *J. Organomet. Chem.*, 2011, **696**, 3745.
44 H.-J. Cho, T. T. Huynh, B. E. Rogers and L. M. Mirica, *Proc. Natl. Acad. Sci. U. S. A.*, 2020, **117**, 30928.
45 D. J. Hayne, J. M. White, C. A. McLean, V. L. Villemagne, K. J. Barnham and P. S. Donnelly, *Inorg. Chem.*, 2016, **55**, 7944.
46 B. Spyrou, I. N. Hungnes, F. Mota, J. Bordoloi, P. J. Blower, J. M. White, M. T. Ma and P. S. Donnelly, *Inorg. Chem.*, 2021, **60**, 13669.
47 A. Noor, D. J. Hayne, S. Lim, J. K. Van Zuylekom, C. Cullinane, P. D. Roselt, C. A. McLean, J. M. White and P. S. Donnelly, *Inorg. Chem.*, 2020, **59**, 11658.
48 L. Sun, H.-J. Cho, S. Sen, A. S. Arango, T. T. Huynh, Y. Huang, N. Bandara, B. E. Rogers, E. Tajkhorshid and L. M. Mirica, *J. Am. Chem. Soc.*, 2021, **143**, 10462.
49 K. Zhou and M. Cui, *J. Labelled Compd. Radiopharm.*, 2017, **60**, 111; L. Fu, K. Zhou, X. Zhang, F. Yi, M. Cui, J. Zhang, B. Xu and J. Tian, *Eur. J. Nucl. Med. Mol. Imaging*, 2018, **45**, S650.
50 F. Yang, K. Wang, K. Zhou, B. Dai, J. Dai, Y. Liang and M. Cui, *Eur. J. Med. Chem.*, 2019, **177**, 291.
51 N. Rastogi, N. Tyagi, O. Singh, B. S. Hemanth Kumar, U. P. Singh, K. Ghosh and R. Roy, *J. Inorg. Biochem.*, 2017, **177**, 76.
52 P. Thapa, S. P. Upadhyay, W. Z. Suo, V. Singh, P. Gurung, E. S. Lee, R. Sharma and M. Sharma, *Bioorg. Chem.*, 2021, **108**, 104681.
53 G. Choi, H.-K. Kim, A. R. Baek, S. Kim, M. J. Kim, M. Kim, A. E. Cho, G.-H. Lee, H. Jung, J.-U. Yang, T. Lee and Y. Chang, *J. Ind. Eng. Chem.*, 2020, **83**, 214.
54 S. Molavipordanjani, S. Emami, A. Mardanshahi, F. Talebpour Amiri, Z. Noaparast and S. J. Hosseinimehr, *Eur. J. Med. Chem.*, 2019, **175**, 149.
55 X. Wang, H. N. Chan, N. Desbois, C. P. Gros, F. Bolze, Y. Li, H. W. Li and M. S. Wong, *ACS Appl. Mater. Interfaces*, 2021, **13**, 118525.
56 S. Jokar, H. Behnammanesh, M. Erfani, M. Sharifzadeh, M. Gholami, O. Sabzevari, M. Amini, P. Geramifar, M. Hajiramezanali and D. Beiki, *Bioorg. Chem.*, 2020, **99**, 103857.
57 J. T. Ryman and B. Meibohm, *CPT: Pharmacometrics Syst. Pharmacol.*, 2017, **6**, 576.
58 J. Fissers, A.-M. Waldron, T. D. Vijlder, B. V. Broeck, D. J. Pemberton, M. Mercken, P. V. D. Veken, J. Joossens, K.

Augustyns, S. Dedeurwaerdere, S. Stroobants, S. Staelens and L. Wyffels, *Mol. Imaging Biol.*, 2016, **18**, 598.

59 M. Vandesquille, T. Li, C. Po, C. Ganneau, P. Lenormand, C. Dudeffant, C. Czech, F. Grueninger, C. Duyckaerts, B. Delatour, M. Dhenain, P. Lafaye and S. Bay, *mAbs*, 2017, **9**, 1016.

60 Z.-X. Wang, L. Tan, J. Liu and J.-T. Yu, *Mol. Neurobiol.*, 2016, **53**, 1905.